# Multiscale modelling of plasma–wall interactions in fusion reactor conditions

# Multiscale modelling of plasma–wall interactions in fusion reactor conditions

## K Nordlund, C Björkas, T Ahlgren, A Lasa and A E Sand

EURATOM/Tekes, Department of Physics, PO Box 43, FI-00014 University of Helsinki, Finland

E-mail: kai.nordlund@helsinki.fi

**Abstract**

The interaction of fusion reactor plasma with the material of the first wall involves a complex multitude of interlinked physical and chemical effects. Hence, modern theoretical treatment of it relies to a large extent on multiscale modelling, i.e. using different kinds of simulation approaches suitable for different length and time scales in connection with each other. In this review article, we overview briefly the physics and chemistry of plasma–wall interactions in tokamak-like fusion reactors, and present some of the most commonly used material simulation approaches relevant for the topic. We also give summaries of recent multiscale modelling studies of the effects of fusion plasma on the modification of the materials of the first wall, especially on swift chemical sputtering, mixed material formation and hydrogen isotope retention in tungsten.

Keywords: multiscale modelling, fusion rectors, plasma–wall interactions, molecular dynamics, rate equations

(Some figures may appear in colour only in the online journal)

## 1. Introduction

In tokamak-like fusion reactors [1, 2] intended for practical power production, the plasma confinement is not—and should not be—perfect. Since the D + T nuclear fusion reaction produces He, which no longer undergoes fusion at a meaningful rate, this He needs to be pumped out from the reactor. All modern tokamak-like reactors are hence designed to have a divertor at the bottom of the reactor, where the He is pumped out, see figure 1 (it is also possible to have another divertor at the top in a so-called double-null configuration, implemented in the EAST tokamak [3]). The plasma properties are such that the divertor is subject to a considerably high (of the order of $10^{20}$ ions cm$^{-2}$ s$^{-1}$) flux of H isotopes with energies of the order of 1–100 eV. Some leakage occurs also at much lower fluxes at the main wall, but the energy of the impinging particles can be much higher, up to the order of 1 MeV [4]. Hence the plasma-facing parts of the first wall are exposed to continuous irradiation by energetic ions and neutral atoms. The whole reactor is at the same time also subject to neutron irradiation that damages the materials [5, 6] but discussion of this topic, although very interesting, is outside the scope of this article.

The effects of energetic ion irradiation on materials have been extensively studied for more than one hundred years [7, 8] due to their relevance for Rutherford scattering [9, 10], ion beam analysis [11], thin film production [12–14], semiconductor technology [15, 16], for example, and most recently the possibility to synthesize and modify nanomaterials with them [17].

Due to the long and extensive study of the effects of radiation on materials, it is known that the irradiation can lead to a large variety of outcomes on the material depending on ion species, energy and the incoming angle as well as the type and temperature of the irradiated material. The initial stage of material modification is known as a collision cascade, and its basic physics is illustrated in figure 2. Many of the known effects resulting from single and multiple cascades are summarized schematically in figure 3. The figure illustrates that the effects which can occur are complex, and understanding them requires a very good understanding of both the penetration mechanisms of energetic particles (essentially a variety of nuclear physics) and materials physics and chemistry.

All of the effects shown in figure 3 can occur in fusion reactors, although some are more likely than others, depending
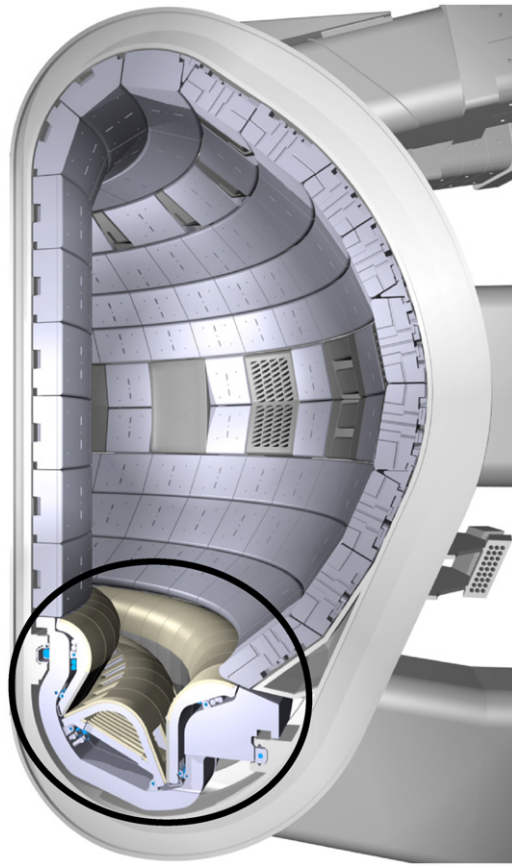
**Figure 1.** Cross section of the ITER [2] tokamak design. The black circle at the bottom shows the divertor region. In the current official design of ITER the divertor plasma-facing parts are composed of C and W, and the main wall is lined with Be. However, very recently the scientific advisory committee of ITER recommended omitting the carbon completely for cost-saving purposes [18].



**Figure 2.** Illustration of the physics of collision cascades. At high kinetic energies ($\gtrsim 1$ keV) an incoming ion and the recoils (black) collide only occasionally and travel in almost straight paths between the collisions. They lose energy during the collision continuously to electronic friction. This phase, which can be described by the binary-collision approximation (BCA) method, leads primarily to point defect production and single atom sputtering. When they have slowed down sufficiently, a dense region of many-body collisions known as a heat spike can form [19–21]. In such regions complex damage such as dislocations [22] and craters [23, 24] can form.

on the design. For instance, in a reactor consisting of only metal parts, amorphous zones do not form (pure elemental metals cannot be amorphized [21]) except possibly in metal alloys that may have formed due to erosion, transport and redeposition. Other effects such as sputtering of the wall material [50], blistering [51] and tritium retention [52, 53] can be very serious problems and possibly even showstoppers for the design of commercially viable fusion power plants. Hence understanding of the plasma–wall irradiation in fusion reactors requires a good understanding of relevant ion irradiation effects on materials.

Fusion reactors are, however, even more complex than a typical ion irradiation setup based on an accelerator, as the sputtering of material from the first wall can change the plasma properties [50, 54], which in turn can change the surface irradiation conditions. Hence the total process is a complex feedback process, and full description requires a combined material and plasma simulation approach. Ultimately, a too high erosion of heavy (high-$Z$) particles into the core plasma can cool it down and extinguish it [2], which of course means that for power-plant operation the erosion must be well controlled. In this review we do, however, focus on reviewing the science of the plasma–material interaction itself, as this already offers a fascinatingly complex and challenging field of study.
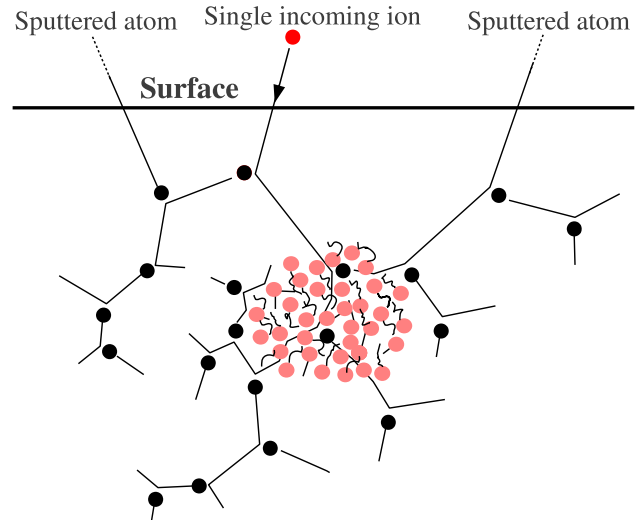
As figure 3 illustrates, the physics and chemistry of plasma–wall interactions is complicated and encompasses more than ten orders of magnitude in time and length scales. The initial ballistic collisions between atoms occur on femtosecond time scales [21], while, for instance, ripple and fuzz formation can take seconds or minutes to become significant [37, 48]. Similarly, even though a single high-energy collision involves impact parameters of the order of 1 Å [55], the size of blisters can be tens of micrometres [42] and strain effects can cause bending of the macroscopic Si wafers [56]. Hence no single material modelling tool can be used to examine all aspects of plasma–wall interactions, and it is natural that multiscale modelling methods have been taken into use to examine them. The concept of how different multiscale simulation methods can be used to model different length and time scales is illustrated in general in figure 4, and also the range that is relevant to the international ITER reactor, currently under construction in the EU, is shown. In a power-plant scale reactor (the first of which is known as DEMO in the current fusion roadmap) the operation times would be so long that the whole time range would be relevant.

In this review, our aim is to provide an overview of the multiscale modelling methods of relevance to fusion plasma–wall interaction modelling, and provide representative recent examples of their use. We do not, however, attempt to provide a comprehensive review of all modelling work on plasma–wall interactions in fusion, as the entire literature is much larger than that which can be included in a relatively concise topical review. The rest of the review is organized as follows. In the subsections of section 2 we present briefly the physical principles of the most commonly used methods
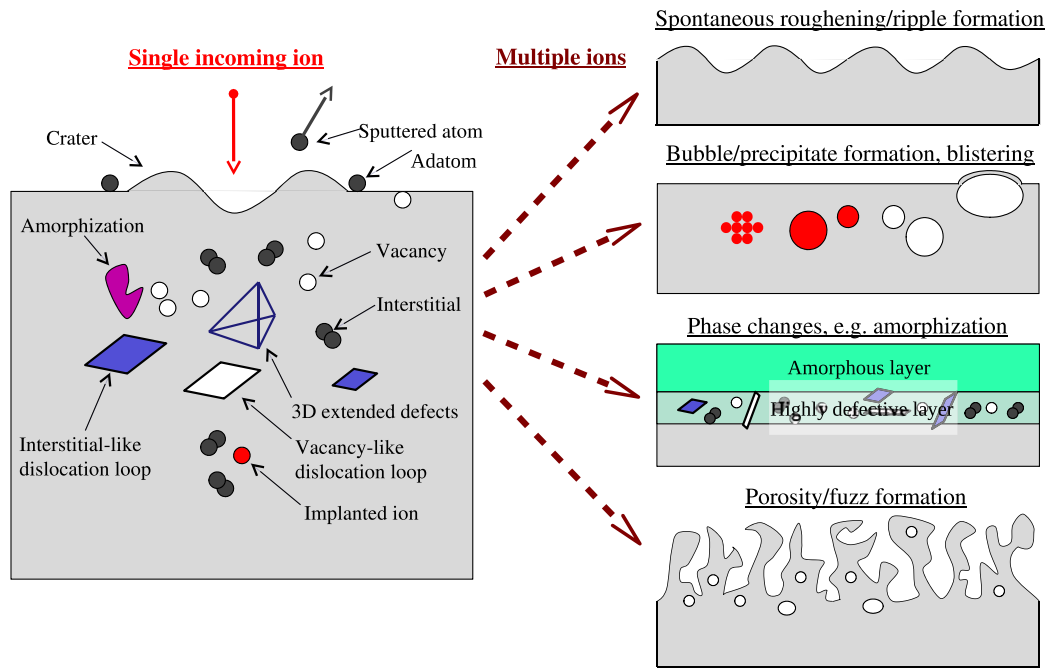
**Figure 3.** Schematic representation of the physical effects that can occur during ion irradiation of materials. Note that a single kind of ion irradiation on the same material cannot lead to all these effects, but this illustration shows the possible effects that are known to occur for some ions on some materials. The left side shows the effects known to occur when a single ion irradiates a material. These include sputtering (atom erosion due to the high energy of the impacting particle) [7, 25, 26], production of point defects [21], cratering [27, 28], implantation [29] and direct formation of extended defects such as dislocations [30, 31], stacking fault tetrahedra [32–34] and amorphous regions [35, 36]. For prolonged irradiation, i.e. when multiple ions impact on the same region of material, several additional effects can result from the damage buildup. Right, top: prolonged irradiation can for certain incidence angles and materials lead to surface nanostructuring in ripple-like forms [37]. Right, second from top: buildup of the implanted ions can lead to formation of precipitates (nanoclusters) and [38, 39], bubble formation [40, 41], which can eventually lead to blisters on the surface [42]. Right, third from top: especially in semiconductors and insulators, radiation can lead to the formation of a continuous amorphous region [43–46]. Right, bottom: some materials such as Ge and W form a highly porous surface layer after prolonged irradiation with certain ions [47–49]—the case of He irradiation in W is now considered a serious issue for fusion reactors.
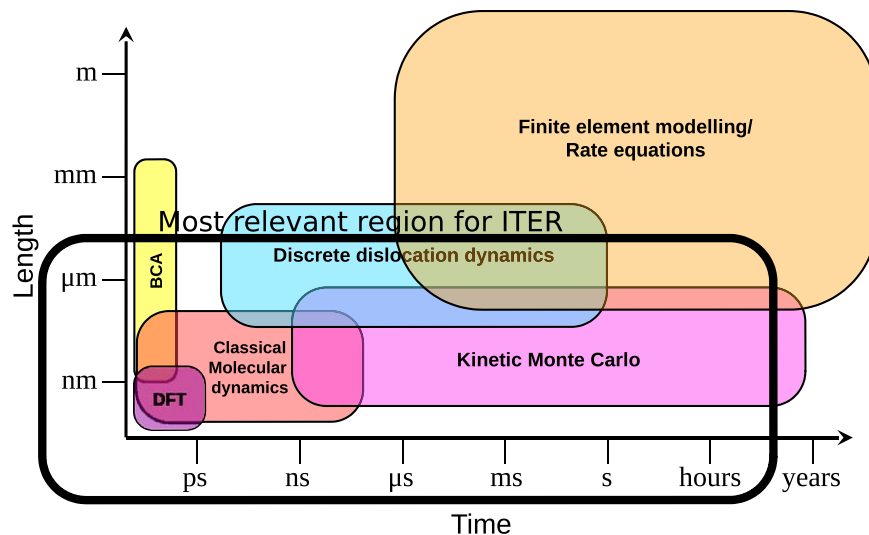


**Figure 4.** Rough description of the approximate time and length scales that can be handled with some of the most common material simulation methods. The inner box emphasizes the point that since ITER will not be a continuously running machine, with respect to radiation effects there will not be a total damage buildup time that would be of the same order as the years relevant to fission and fusion power plants. For the same reason it is unlikely the damage effects would build up to macroscopic length scales. All the methods are described at length in the main text.

in current irradiation materials science, comment on their relevance to fusion plasma modelling, and provide references for readers wanting deeper information. In section 3 we describe the swift chemical sputtering (SCS) mechanism that

has proven to be highly relevant specifically for fusion plasma–wall interactions. In section 4 we discuss the formation of mixed materials, which is a serious issue in reactors due to the redistribution of plasma impurities. Finally in section 5

we discuss how atomistic simulation tools can be combined with rate equations to model H behaviour in reactor W on macroscopic time scales.

## 2. Multiscale modelling

### 2.1. Density-functional theory (DFT)

The DFT approach [57, 58] is based on two theorems by Hohenberg, Kohn and Sham, which state that (1) the ground state energy of a non-degenerate electronic state is a unique functional of its density and (2) the energy can be obtained by variation of the universal density functional with respect to the charge density. This implies that calculation of the wavefunction of a many-electron system is not required in order to find the total energy, but that it is enough to know only the charge density. This leads to a major reduction of the computational complexity compared to solving the true all-electron Schrödinger equation. However, the exact density functional is not known, and many different approximate functionals are used instead. Often these are chosen based on what compares best to experiments, and thus DFT is not necessarily a fully *ab initio* method in the sense of using no empirical input.

DFT-based and other quantum mechanical methods have a high accuracy but are computationally very expensive; simulations are normally limited to systems composed of a few hundred atoms and picosecond time scales (see figure 4). This makes the use of such methods impractical for tackling most radiation-related problems, e.g. formation of defects in collision cascades or direct dynamical simulations of defect diffusion. However, in some limited low-energy cases, direct quantum mechanical simulation of radiation-induced defect production has been achieved [59–61]. More commonly DFT is used to obtain the energies and diffusion behaviour of defects (for a few examples in different classes of materials see e.g. [62–72]), which can be very useful for examining H and He behaviour in fusion reactor materials. An example of such usage is given in section 5.

### 2.2. Binary-collision approximation (BCA)

The BCA is the oldest computer simulation approach for calculating the passage of ions in solids [55, 73]. In this approach, the passage of an ion in a material (solid, liquid or gas) is calculated as a sequence of independent binary collisions by solving the classical scattering integral for purely repulsive interatomic potentials [55, 74]. The BCA code TRIM/SRIM [75–77] is widely used in the ion irradiation field due to its convenient graphical user interface and extensive database of electronic stopping powers. It (as well as most BCA codes developed specifically for fusion simulations [78, 79]) uses a random ('Monte Carlo') algorithm to select the impact parameter of the next colliding atom as well as its type. The solution of the integrals of motion results in precise scattering angles for both the projectile and the target atom. Hence it can describe fairly accurately amorphous materials. Some BCA codes can also describe crystals, such as MARLOWE [55, 80] and 'Crystal-TRIM' [81].

The BCA method has several limitations. It is not able to distinguish when a cascade goes over from the linear cascade to the heat spike regime, but keeps treating the collisions as independent binary collisions regardless of the collision density. Because of this, its range of physical validity for single ions is limited to sub-ps time scales (see figure 4). Although it can be used to estimate damage production (basically by counting recoils that exceed the threshold displacement energy) [82], it cannot reveal anything about the atomic structure of these defects. The description of sputtering or other surface effects (important in nanosystems) is problematic as the inherent algorithm does not have a unique way of describing the atom binding at surfaces [83, 84]. Nevertheless, BCA often gives reasonable deposited energy and range distributions and primary recoil spectra for a wide range of materials [79, 85–91], and it is orders of magnitude more efficient than a molecular dynamics (MD) simulation.

Due to its efficiency, the BCA method is of particular interest for the fusion community because of at least two reasons: it can be coupled concurrently with plasma simulation codes such as ERO [92], and it can (together with appropriate statistics-collecting algorithms) be used to track material mixing due to ion implantation and surface composition change due to preferential sputtering. The BCA code TRIDYN [78] was developed particularly for simulating composition changes as a function of depth [86, 93, 94], and its successor code SDTrimSP [95] can do this also as a function of lateral surface position and height.

### 2.3. Molecular dynamics (MD)

In MD, Newton's equations of motion are numerically solved to determine the time evolution of a system of interacting objects [96, 97]. It is a very widely used method to study all kinds of atomic-level physics, chemistry and biological issues [98, 99], and by no means specific to radiation effects. For simulation of radiation effects, the basic MD methods [96] need to be amended with a few solutions specific to radiation effects. These include accounting for electronic stopping as a frictional force [100], joining the equilibrium interatomic potentials with realistic high-energy repulsive interactions [75], and making the time step adaptive to the maximum kinetic energy and force in the system in the ballistic phase of the cascade [100] while reducing it to a normal constant equilibrium time step after the cascade. Also, the radiation effect simulations cannot be carried out in any thermodynamic equilibrium ensemble as the initial collisional stage is not a thermodynamic system at all because the collisions occur faster than the relaxation time of the solid. Hence typically the central part of the system is treated by direct solution of Newton's equations of motion, while the boundary regions far from the collision zone are cooled down to remove the excess energy introduced in the system [17, 101].

MD is very well suited to examine the nuclear collision and heat spike aspects (see figure 2) of primary radiation damage, as with current computers it is possible to simulate the entire extent of collision cascade evolution both in space (up to length scales of hundreds of nanometres in three dimensions) and time

(up to nanoseconds) [102]. MD simulations require forces as the starting point for solving the equations of motion. The forces can be obtained directly from DFT or with classical interatomic potentials. As DFT MD simulations are still limited to a few hundreds of atoms [61], classical (empirical, analytical) potentials remain the method of choice for high-energy radiation effect simulations, as these typically involve at least tens of thousands of atoms.

Potentials exist for a wide range of systems and purposes. However, when simulating radiation effects, it is crucial to select potentials that allow for bond breaking and reformation, ruling out the use of most molecular mechanics force fields [98]. For carbon-based systems, the Brenner potential [103] and its extensions [104, 105] as well as the ReaxFF formalism [106] allow for bond breaking. The Brenner potential has proven to be quite useful for modelling the effects of fusion reactor hydrogen isotopes impacting on carbon-based reactor materials [60, 107–115], as will be discussed further in section 3.1.

For metals, the Finnis–Sinclair and embedded-atom method potentials and their functional equivalents are widely used, [116–120] while for covalently bonded materials Tersoff-like bond-order potentials [103, 121, 122] have proven to be quite successful. For compounds of different types of materials, far fewer potentials are available, but since the Tersoff and Finnis–Sinclair-like potentials are fundamentally similar [103, 123], a Tersoff-like formalism has proven to be useful in the development of potentials for carbides, oxides and nitrides [123–127].

To enable fusion-reactor plasma–wall interaction modelling in an ITER-like environment involving Be, W and possibly also C, interatomic potentials for the entire Be–W–C–H quaternary system in the Tersoff-like potential formalism [126, 128, 129] have been developed, using the well-tested Brenner potential for C–H [103] as a basis. The specifics of this potential will be discussed in section 4.2.1. Later specific potentials better optimized for W and W–H have been added to the list of ITER-relevant potentials [130, 131].

## 2.4. Kinetic Monte Carlo (KMC)

The main limitation of MD is the time scale. The MD time step is of the order of 1 fs, and cannot be increased in a general non-equilibrium situation. For systems involving well-defined transitions from one state to another, several speedup schemes exist [132–134], however, these do not generally work well in amorphous materials. This limits most MD simulations to nanosecond time scales. As a direct consequence, most diffusion and other long-time scale evolution processes are not accessible by MD.

KMC methods can sometimes solve this problem [135–138]. The method takes as input the rates of relevant processes in a system, which typically are the defect migration rates and flux of incoming ions, and simulates the time evolution of the atoms or objects. The algorithm selects the processes proportional to their rates, so no computational capacity is lost in time steps with no events occurring.

The time in KMC advances stochastically, but on average as $\Delta t = 1/R$ where $R$ is the sum of all rates $r_i$ in the system.

Hence if fast-moving objects vanish from the simulation due to e.g. recombination, the high values of $r_i$ vanish from the sum $R = \sum r_i$. This makes R decrease and hence the time advancement $\Delta t$ increase. Thus a KMC simulation may speed up in the evolvement of real time as a system develops, which is a major advantage to simulations.

There are many varieties of KMC. In atomic kinetic Monte Carlo (AKMC) simulations all atom coordinates are included but only one or a few defects (typically vacancies) at a time are moving [139]. In other modifications of the method, only the mobile defects are followed, and the lattice atoms are not explicitly described at all (such methods are known as object, reaction, event or first-passage kinetic Monte Carlo, i.e. OKMC [140, 141], RKMC, EKMC [142] or FPKMC [143], respectively). Since only the objects of interest are simulated, this allows for simulation of macroscopic time (up to several hours) and length scales.

KMC simulations have been used to examine many aspects of hydrogen diffusion in fusion first wall-relevant conditions, especially for carbon-based materials [144–146] and W [139, 141, 147, 148]. We consider it likely that the use of different varieties of this group of methods will further increase as knowledge of the defect diffusion properties needed as the input for KMC keeps increasing.

## 2.5. Discrete dislocation dynamics (DDD)

DDD aims to model the behaviour of dislocations [149, 150] by describing a dislocation line as a sequence of connected line segments. These line segments interact with each other via their strain fields, which for isotropic materials are known analytically [150]. Taking into account crystal anisotropy is challenging, but advances have been made towards this goal recently [151, 152]. Once the interaction strength is known, the motion of dislocations is solved with the same basic principle as atom motion is solved in MD. The segments are given a fictitious mass that gives them reasonable velocities compared to experimental observations.

DDD is in principle a very powerful tool to predict the mechanical response of materials (especially metals where dislocations dominate the mechanical behaviour on the macroscopic scale) to external deformation, and some studies have given an insight into the plastic behaviour of materials [153]. Unfortunately the knowledge of dislocation reactions and formation mechanisms needed to parametrize DDD is incomplete. Hence currently there are extensive activities ongoing to use MD modelling to determine dislocation reactions that can be used to develop the DDD methods further, see e.g. [154–157].

DDD is not likely to be of major relevance for plasma–wall interactions in ITER, as the total radiation doses there are not high enough to induce major mechanical property changes in the W. However, at the DEMO/power plant stage, major material modification at the divertor is expected due to the combined ion and neutron fluxes [148]; DDD will also likely be used for plasma–wall interaction modelling.
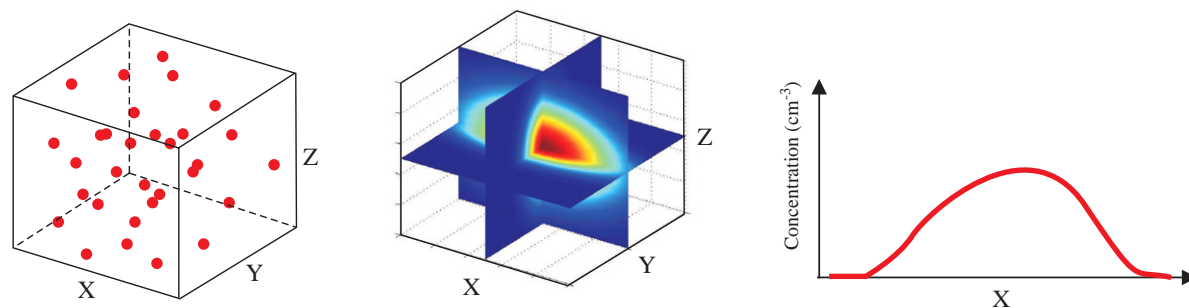
**Figure 5.** In RE, the positions of the wanted entities are represented as concentration profiles. Usually, only a solution in one dimension is needed.

## 2.6. Rate equations (RE)

To be able to simulate long time (seconds to years) and large volume (corresponding to $>10^{15}$ atoms) processes, so-called rate equations (RE), also called *rate theory*, can be used. The RE formalism comes from the *continuity Equation*, *transition state theory* [158, 159] and the *theory of sink strengths* [160, 161]. The positions of the considered defects, atoms or impurities are transformed to concentration distributions, see figure 5, and these are solved numerically. Note that the inputs to RE modelling are from a physical point of view essentially the same as those for KMC (albeit used in a different form). As RE are a fully continuum method, they have the advantage that they can treat fully macroscopic time and length scales, at least for 1D profiles. To simulate a system with 3D information of the system state, rate equations become computationally challenging.

The number of atoms versus simulation time for different simulation methods are summarized in figure 4, but note that the rapid increase in computational capacity changes this estimation continuously. Section 5 gives an example of the use of rate equations for fusion modelling.

## 2.7. Finite-element modelling (FEM)

The basic idea of FEM of materials is to describe an object of arbitrary size as a set of connected triangles (2D) or prisms (3D). The size of these prisms can change based on an external mechanical load in a way that is consistent with the elastic constants of a material. In its basic implementation, FEM can simulate elastic deformation of materials, both for isotropic and anisotropic materials, and can for known elastic constants achieve an arbitrarily accurate solution of the elastic deformation. The size of the prisms can be widely varying in different regions of space and there is no inherent limit to what their size can be, which makes FEM well suited to study macroscopic objects. Moreover, with algorithmic extensions and proper parametrization from experiments or lower level methods, FEM can be extended to also describe plastic deformation [162, 163].

The major limit of FEM is that it does not consider any information of the atoms, although it is possible to make a multiscale combination of FEM and atomic simulations like MD [164–166].

FEM is very widely used to examine the mechanical properties of macroscopic objects, and is a standard tool in the materials manufacturing industry. In this respect, the design of the entire ITER reactor is strongly dependent on FEM, and it can also be used to model e.g. the change of the mechanical size of the divertor components due to thermal expansion under the heat cycling of ITER. Since the heat is coming from particles (electrons, ions and light) escaping the plasma, in one way FEM modelling is also relevant to fusion plasma–wall interactions. In the more focused sense of this article of considering material damage by plasmas, FEM is also relevant for modelling the macroscopic behaviour if the changes of the mechanical properties by radiation are taken into account in a FEM model. However, as noted above for DDD, ITER is not likely to be subject to major changes of the mechanical response, and hence the radiation damage plasma–wall relevance of FEM will be more significant at the DEMO/power plant stage.

## 3. Swift chemical sputtering

### 3.1. Carbon and other covalently bonded materials

The bombardment of carbon-based materials by low-energy (1–100 eV) H isotopes (H, D or T) is still of great interest in nuclear fusion reactors, since carbon composites were for a long time considered the materials of choice for the first reactor wall, are still used in several existing reactors such as JT-60 [167], and will be used in future machines such as the Wendelstein-7X stellarator [168]. Carbon in different graphitic forms has several advantages for fusion, such as a very good thermal stability up to high temperatures, relatively low cost, and low atomic number $Z$ (impurities in the main fusion plasma cool it down by $Z^2$–$Z^4$ depending on which process is considered). Experiments have shown that the lowest part of the reactor, the divertor, is eroded by the incoming H due to sputtering of hydrocarbon molecules [169–176]. The mechanism behind this effect was for a long time unclear [173, 177] since at the lowest energies (1–10 eV) physical sputtering of the wall is impossible.

At high temperatures it is known that H atoms can enter the amorphous hydrogenated carbon (*a*-C : H) samples and change locally the bonding structure, resulting in the formation of a weakly bound molecule which can migrate to the surface and desorb [54]. This requires thermal activation, however, and hence it cannot explain the observation that the
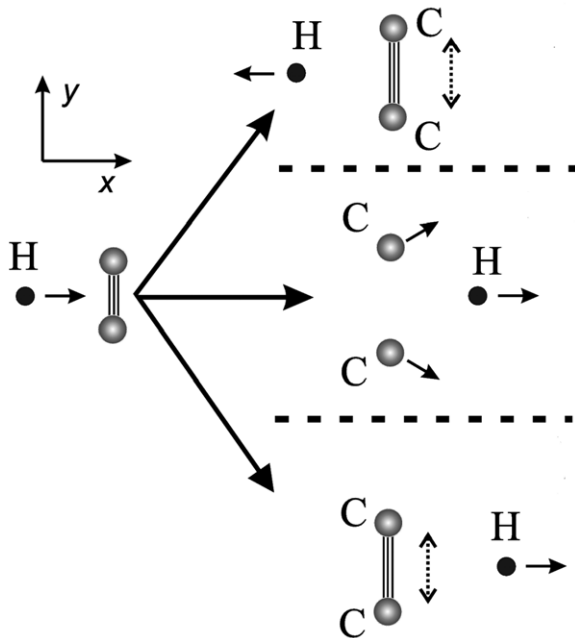
**Figure 6.** Schematic representation of the swift chemical bond breaking in a carbon dimer. Depending on the energy three different outcomes are possible. Top right: incoming energy too low, hydrogen does not penetrate bond, no bond breaking. Middle right: suitable energy, hydrogen penetrates bond and slows down so much there is sufficient time for bond breaking. Bottom right: hydrogen penetrates bond rapidly, there is not sufficient time for momentum transfer, and bond does not break. Adapted with permission from [60], Copyright 2002 Elsevier.

desorption rate is the same between liquid nitrogen and room temperature [178].

Through using MD simulations of the bombardment process, a new kind of chemical sputtering mechanism, which can lead to the instantaneous erosion of hydrocarbon species from surfaces, has been discovered [60, 107–109]. The nature of the mechanism is easiest to understand by considering the model system of one H atom colliding with a C–C dimer. The most symmetric case possible is the one where the H atom moves perpendicular to the chemical bond towards the middle of it, see figure 6. The momentum transfer in the $y$ direction can be calculated [60] as

$$p_y = \int_{-\infty}^{\infty} f_y(t, E_{\text{kin}}^{\text{H}}) \, dt \approx \bar{f}_y \bar{\tau}, \qquad (1)$$

where $f_y$ is the force acting on the carbon atoms and $E_{\text{kin}}^{\text{H}}$ the initial kinetic energy of the H atom. To enable easier understanding, the integral is simplified to be a product $\bar{f}_y \bar{\tau}$, where $\bar{f}_y$ is an effective average force during the collision, and $\bar{\tau}$ the effective average time the H atom spends in the area of the C–C bond.

If the kinetic energy of the H ion $E_{\text{kin}}^{\text{H}}$ is low, the H atom returns without entering the region between the C atoms. Then $\bar{f}_y$ and the $y$ momentum are small and the bond is not broken (figure 6 top). When the initial kinetic energy of the impinging particle is high enough for the H atom to stay for a (relatively) long time $\bar{\tau}$ in the region between the atoms, the bond breaks

(figure 6 middle). If the initial kinetic energy is even higher, the bond breaking ceases (figure 6 bottom). This is because, although $\bar{f}_y$ is large, the particle spends too little time between the carbon atoms to cause any bond breaking ($\bar{\tau}$ is short). Thus there is a finite energy window in which bond breaking can occur. The characteristic time of this process is very short, of the order of 10 fs. Because the mechanism involves atom bonding, requires kinetic energy and is rapid, it has been named 'swift chemical sputtering' [179].

To rule out the possibility that the mechanism is an artefact of a particular interatomic potential, it has been shown that the effect occurs as described above using three varieties of the Brenner potential [103–105], as well as in a tight-binding quantum mechanical framework which is completely independent of the classical simulations [60]. This model system was also examined with He, and found that it can also lead to bond breaking, albeit with a clearly lower cross section.

In addition to the study of the dimer model system, extensive simulations of H, D and T bombardment of actual *a*-C : H material have been carried out. The main results obtained can be summarized as follows. It was shown that the SCS mechanism leads to sputtering of small hydrocarbon molecules down to energies of about 2 eV, and that the sputtering yields obtained are in the experimental range of yields [109, 110]. It was also observed that the sputtering yields are highly sensitive to the detailed surface structure [180], and that for high fluxes a H supersaturation can form on the surface, which can reduce the C sputtering by an order of magnitude [107]. These observations explain experimental results on the same systems. The temperature dependence of the sputtering yield was also examined, offering a possible explanation to why the yield had a maximum at about 700–900 K [109] (although the so-called Küppers cycle [54] is certainly also active at these high temperatures). Most recently, we have found that even if 10% of the bombarding particles are He, Ne or Ar, with the *same* energy as the incoming H, the erosion yield does not change appreciably (more than ∼10%) compared to the case of bombardment with H only [181].

Several groups have carried out similar simulations of H bombardment of carbon-based materials and found essentially the same mechanism to be active [111–113]. These simulations have also revealed several other aspects of the SCS mechanism carbon, such as its angular dependence [112], effect of electronically excited states [114], cobombardment with plasma impurities [115], high-flux effects [182], isotope effects [183], as well as the effect of sample structure [111]. The simulated yields have also been found to be in good agreement with experiments [110, 113].

Also the effect of the doping of carbon materials with other elements on sputtering have been studied [184, 185]. For instance, several studies have shown that Si concentrations around (5–10 at%) reduce chemical sputtering yields by a factor of 2–3 compared to pure graphite [186–189]. This effect was qualitatively reproduced in MD simulations [190].

Although reduction of the SCS carbon erosion yield is thus possible, the effect is essentially impossible to avoid for covalently bonded materials as it only requires a single H isotope of suitable energy to penetrate between two carbon

atoms. This leads to the fact that any carbon-containing reactor will always suffer some erosion in the form of hydrocarbons. These can drift elsewhere in the reactor and redeposit, leading to the buildup of tritium-containing thin films [93] which are very difficult to remove, and can lead to the legal limits for tritium inventory to be exceeded [50, 53, 191]. This is the reason why carbon is not considered to be used in the D+T phase of ITER.

All of this work focused on carbon due to its importance in fusion reactors. Since our argument for how the bond breaking occurs is a very generic one and the time-dependent bond breaking argument is in no way specific to carbon, however, it is reasonable to assume that it might also occur in other covalently bonded materials. As a test case, Si was considered, and it was shown that it does, indeed, also sputter by the same mechanism [192].

### 3.2. Metals

*3.2.1. Dimer model applied to metals.* Since SCS involves bond breaking, the authors finding it originally believed that it is natural only to covalent materials and that it would not occur in metals due to their non-directional bonding [192]. Later, the same authors found that applying the dimer model described above to the Be dimer, a similar bond breaking occurs [193, 194], indicating that SCS could also be present in the metal Be. (A bond in metals is here defined as the attraction between lattice atoms.) The difference compared to the C dimer breaking lies only in the lower required energy, due to the different bond strengths. Even the mixed Be–W and Be–C dimers are seen to break when a H isotope penetrates in between the atoms. Bond breaking for a pure W material is, on the other hand, highly unlikely due to large mass differences between the H and W atoms and related weak momentum transfer [193, 195].

A real surface is naturally very different from a collection of dimers. For instance, the coordination number $Z$ of atoms located at the surface changes during irradiation (in the case of Be, it could range from only 1 to the ideal surface coordination $Z = 9$ or bulk hcp $Z = 12$), atoms can be manifold connected to not only other substrate atoms but also to added plasma or impurity atoms. Hydrocarbon chains are common on hydrogenated carbon surfaces, sub-surface bubbles can form and the surface can be depleted on substrate atoms if the incoming ion flux is very high. All of this affects the ability of the substrate atom to be sputtered and a break-up during the simple dimer simulations does not therefore by default lead to actual Be sputtering through the SCS mechanism.

*3.2.2. MD simulations of chemical sputtering in Be.* Moving from the dimer model to modelling a real surface irradiation event is possible by simulating bombardment of small surface slabs using MD (a typical cell contains a few thousand atoms). The simulations are done either cumulatively or non-cumulatively. The cumulative simulations are performed to mimic an evolving surface but due to extensive computational cost per impact, the flux and fluence of the incoming ions are usually restricted to a few thousand bombardments impacting

at a flux of $\sim 10^{28}\,\mathrm{m}^{-2}\,\mathrm{s}^{-1}$. A uniform bombardment of the surface is simulated by shifting the cell randomly in the $x$ and $y$ directions ($z$ is defined as the surface coordinate and is non-periodic) before each impact and allowing the whole cell to relax at a chosen temperature in between. Fixing the bottom atom layers keeps the cell in place and an infinite lattice is mimicked by keeping the cell borders at the desired temperatures at all times. Lengthy calculations are avoided when performing non-cumulative simulations. The surface evolution is then not of interest, but the focus is shifted to the interaction between a pure surface (alternatively a somehow prepared/modified or amorphous surface) and the irradiating species in an equilibrium situation. The two methods may give differing results, for instance, when the impurity surface concentration plays a role [196].

Simulating D irradiation of Be surfaces reveals that SCS is indeed present in Be and furthermore an important erosion mechanism [197]. The release of BeD molecules at low impacting ion energies, 7 eV, is the result.

Snapshots of a sputtering event where a 10 eV D ion is bombarding a Be surface is illustrated in figure 7. At the end, the incoming D ion is sputtered away as part of a $D_2$ molecule and energy analysis shows that is has lost more than 90% of its initial kinetic energy. This loss of energy is a gain in potential energy of the Be atoms with which it interacts. Between figures (*a*) and (*b*), the D ion collides with a Be atom, losing about 6 eV in the process. The rest of its kinetic energy is lost when it penetrates in between the Be atoms in (*c–e*). In total, the D ion has caused five Be–Be bonds to break. Initially, four D ions were neighbours to the sputtered Be, but only one of these (number 2 in the snapshots) was sputtered together with the Be (a neighbour is defined as an atom inside the cutoff range of the potential).

The top surface structure, or more precisely the neighbouring surroundings of a Be surface atom, is a highly important factor in the sputtering process. Since a 7 eV D ion is able to sputter a Be atom, the Be atom must be weakly bonded to the surface. This indicates that is has only a few bonds to other Be surface atoms. Example energies per bond in the above-mentioned simulations for a surface Be atom with 9 Be neighbours are, on average, $0.30 \pm 0.01$ eV and with 6 Be neighbours $0.36 \pm 0.02$ eV. Calculating the same energies when a few D bonds are present results in: 9 Be and 2 D bonds = $0.25 \pm 0.01$ eV, 6 Be and 3 D bonds = $0.28 \pm 0.02$ eV [197]. At low bombarding energies, the number of initial Be neighbours to the sputtered Be atom is less than the amount in high-energy cases where it reaches the ideal of 9 of a hcp $(0\,0\,0\,1)$ surface, which is explained by the larger penetration depths of the D ions at higher energies. Due to the same reason, the number of D neighbours shows the opposite trend, meaning that the Be atoms in the low-energy bombarding cases have a higher possibility to be weakly bonded to the surface and as such also to be easily eroded.

The mean release energy of BeD is around 2 eV, agreeing with observations that the molecules are released with much higher energy than that corresponding to the surface temperature [198]. Their release angles form a cosine distribution around the surface normal.
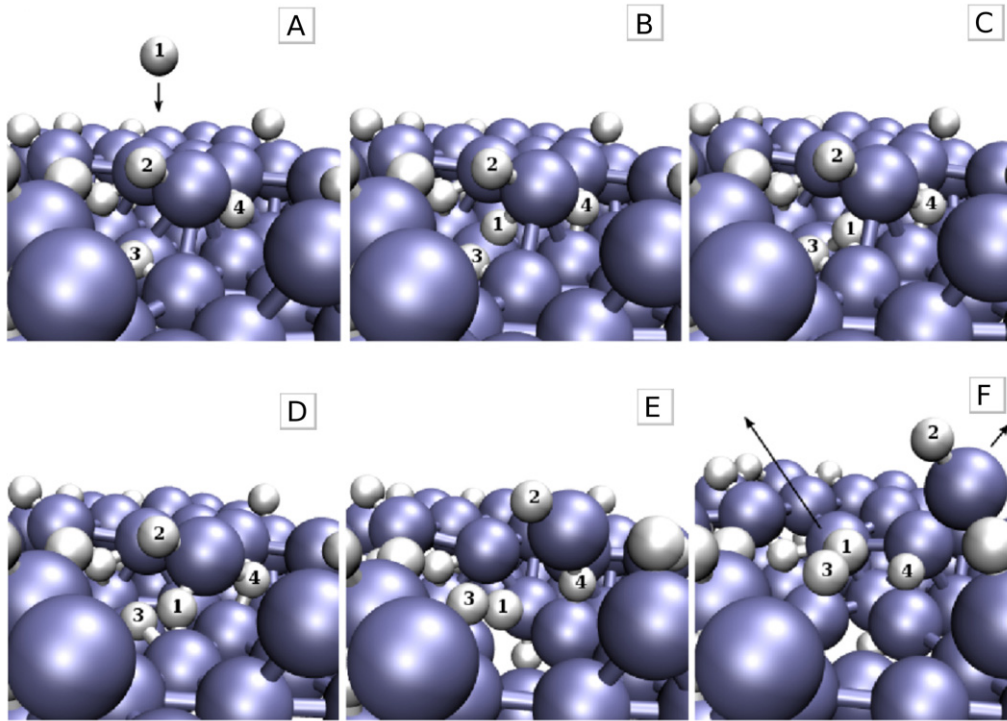
**Figure 7.** Snapshots at six different times during a sputtering event. The D ions are represented by the small light grey spheres and the Be atoms are the larger dark spheres. The arrows in the last snapshot (F) show in which direction the sputtered $D_2$ and BeD molecules are moving.

The chemical sputtering, here defined as the release of BeD molecules from the Be surfaces, is hence an essential factor in the low-energy bombardment regime. At 7–20 eV, the fraction of Be sputtered as BeD molecules (including $BeD_2$) can be as high as 100% (see figure 8). As the impact energy increases, Be atoms are also released via physical sputtering, lowering the BeD molecular fraction.

Performing non-cumulative simulations of D impacting on a pure Be surface would result in a much higher sputtering threshold than in the cumulative case [196]. This is due to the lack of D ions accumulated in the surface, meaning that all Be atoms are strongly bonded to the surface and therefore require relatively high kinetic energy to be released from the surface. Non-cumulative simulations using surfaces with added D (e.g. taking the final cell structure after cumulative bombardments), result in a more realistic threshold. Using cells corresponding to any real fusion reactor wall element or experimental sample would be ideal, however, parameters such as the structure of and D content in the samples are often difficult to quantify and therefore not well known.

BeD molecules are also released from BeW surfaces during MD simulations [194]. The addition of W in the surface makes the contribution of the chemical branch less prominent compared to pure Be surfaces, especially if the top layers are dominated by W, which could be a result of preferential sputtering of the lighter element Be.

*3.2.3. Experimental observations of BeD molecules.* BeD molecules have also been observed during experiments, both in the linear plasma device PISCES-B [198] and in the tokamak
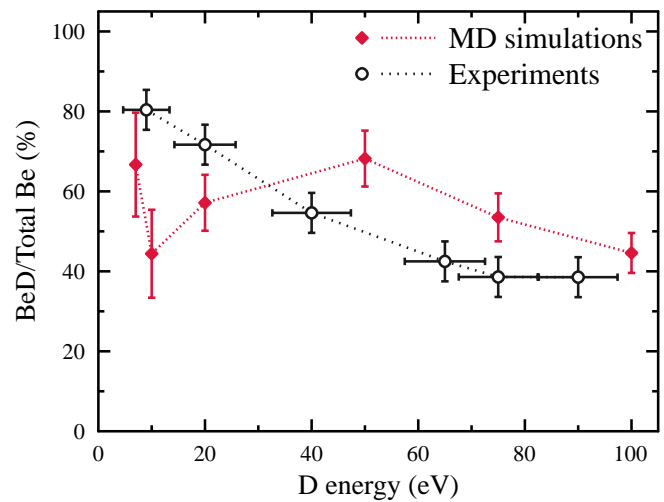


**Figure 8.** The fraction of Be sputtered as BeD molecules as a function of incoming D ion energy during MD simulations and measured in the PISCES-B facility [199].

JET [200, 201]. In PISCES-B, the molecular release has been found to be dependent on the incoming D ion energy, showing a similar trend as in the MD simulations (see figure 8), but also on the surface temperature of the exposed Be sample. At high temperatures, the BeD spectroscopic signal, and hence the contribution to the sputtering coming from the molecules, is seen to decrease in comparison to lower temperatures. This has been related to the decomposition of $BeD_2$ molecules on the Be surface. After a peak at around 440 K, $D_2$ molecules are released from the beryllium hydride ones and therefore lower the chance of BeD release [198].

Recent observations in JET also support this temperature dependency [191]. When measuring the BeD signal from Be tiles in the first wall, a significant intensity drop is observed between surface temperatures of around 500 and 700 K. Gas balance calculations have revealed that the chemical sputtering contribution, i.e. the BeD molecular fraction of the total sputtering, was around 33% at 75 eV impact energies, which agrees well with both simulated and measured PISCES-B values.

*3.2.4. Multiscale modelling of Be irradiation experiments.* Modelling efforts to tie the MD simulations and experimental observations of the BeD molecules together have been done by using the 3D plasma impurity code ERO [92, 194, 202, 203]. ERO follows particles that are either physically or chemically eroded from different surfaces of a fusion device due to impinging plasma ions (fuel or impurities). The released particles enter the plasma as neutrals but at each time step, the ionization (or dissociation) probability is calculated, which depends on the local plasma parameters (electron density and temperature) and calculated reaction rates. Once ionized, the movement of the ions is affected by the magnetic and electric fields. Also friction with the background plasma, thermal forces and diffusion are taken into account. The eroded particles can return to the surface and be reflected or cause additional sputtering or simply escape from the simulation volume.

The ERO code has been applied for modelling PISCES-B experiments aimed at quantifying the Be and BeD appearance near a Be target exposed to a D plasma. The light emission from both neutral and ionized Be and the BeD band (497.3–499.2 nm) was spectroscopically measured and the plasma parameters (electron temperature and density) and target bias voltage were varied [194, 203]. The temperature of the target was not regulated.

MD data were used for determining the physical and chemical sputtering yield in the ERO simulations. Assuming that the contribution to the total sputtering from the BeD branch decreases from 100% at low impact energies to only around 20% at higher energies, resulted in an overestimation of the sputtering when compared to the experimental observations [203]. However, since the surface temperature of the Be target was allowed to vary throughout the experiments, the chemical branch did not follow the above trend obtained for a sample kept at constant temperature. Instead, it showed a constant fraction at all impact energies (applied bias voltages) of around 17%. Assuming this fraction in the simulations resulted in better agreement [194].

Both the simulated and the measured profile of neutral BeD light as a function of distance from the Be target in the PISCES-B device is shown in figure 9. The figure illustrates that the penetration of simulated BeD molecules in the plasma is only slightly smaller than what is observed. The small differences could be explained by an overestimation of the assumed ionization and/or dissociation rates. In addition, since no reaction rates for this are available, the ERO simulations did not include volumetric formation of BeD through endothermic reactions between $Be^+$ and $D_2$ [198], which could also add to the differences.
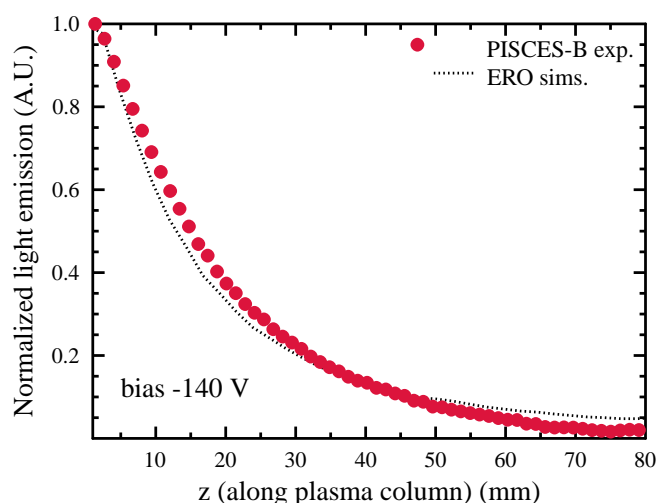


**Figure 9.** The normalized light emission intensity of the BeD band. The circles represent PISCES-B experimental results and the dotted line is simulated results. The target bias voltage was −140 V. The data is from [194, 203].

# 4. Mixed material development

The material that is released into the fusion plasma as a consequence of the plasma–wall interactions will mostly return to the wall and thus reduce the gross erosion. However, part of the eroded species may migrate long distances and upon redeposition form layers of co-deposits and so-called mixed materials, whose composition and structure distinctly differ from the initial wall material. The co-deposits may also contain, in addition to the different wall materials, fuel atoms, i.e. hydrogen isotopes. The impact of these mixed materials on fuel retention and the possible increase of erosion and degradation of the thermo-mechanical properties of such layers are issues that need to be addressed when assessing the lifetime of a fusion reactor.

Simulations provide an insight into the formation of these mixed materials on an atomic level and also give information about their erosion behaviour and retention capabilities.

## 4.1. The carbon–tungsten system

Mixing W and C results in either the carbide WC or the subcarbide $W_2C$. Which carbide is formed depends on the temperature, as annealing evaporated C on tungsten substrates at 970 K shows that $W_2C$ is the dominating phase, until it is converted into WC at 1270 K [204, 205].

Inai *et al* [206] have studied 10 eV–1 keV C bombardment of initially crystalline W surfaces using both MD and KMC in order to quantify the C deposition and reflection. At low energies, a C layer is seen to form on top of the W surface. At the highest energies, a mixed 'hybridization layer' is formed, which, however, does not exhibit any crystallinity or particular ordering. A steady-state condition with constant sputtering of the deposited C and bulk W atoms is reached for this mixed layer and its C sputtering is larger than that of the deposited C layer. Atomic scale roughness not included in the KMC calculation were the cause for different results concerning the C deposition modelled with MD and KMC.

The sputtering of WC layers due to hydrogen isotopes has been studied using MD simulations [195, 207–209]. WC is an interesting system due to the large atom size and mass difference of the constituents, and MD simulations of radiation of bulk WC showed that this leads to a major elemental asymmetry in the damage production [207, 210]. Hence it is not surprising that also the plasma–wall interactions show major elemental asymmetries. Cumulative bombardments of both crystalline and amorphous WC surfaces with deuterium showed that for all ion energies used (up to 1 keV), the erosion of tungsten is negligible which is equivalent to the preferential sputtering of carbon leading to a buildup of W atoms in the surface [207, 208], agreeing with experimental findings [94].

Other findings from the simulations [195, 207–209] include the fact that the tungsten sputtering is not enhanced for WC surfaces compared to pure W ones. The C sputtering yields, on the other hand, are of the same order of magnitude for C and W terminated surfaces, but the former can be larger by as much as a factor of 4, since the carbon atoms in the first surface layer can react more easily with the incoming deuterium ions. Sputtering is seen at impact energies as low as 10 eV, indicating that chemical sputtering, through the SCS mechanism, is present, at amounts similar to that of pure C surfaces. Furthermore, the initially crystalline surfaces are amorphized during the cumulative bombardments. This amorphization is most pronounced at D energies of 100 eV, where the D retention also is the largest. The retained D, of which 33–48% are bound as $D_2$ molecules in the sample, hence facilitates the amorphization. Non-cumulative bombardment of amorphous surfaces with different W content also showed preferential sputtering of C, but with a decreasing yield as the W content increases.

### 4.2. The carbon–beryllium system

Only one intermediate phase of beryllium carbon has been reported [211]. This phase is the ionic $Be_2C$ cubic antifluorite structure, which can be described as carbon atoms occupying fcc sites and beryllium atoms forming a cubic sublattice inside. In this way, each C atom is surrounded by eight Be atoms.

The carbide phase has been observed to form during 5 keV $C^+$ irradiation of clean Be surfaces [205, 212]. A high fluence is needed to reach the necessary stoichiometry for carbide formation, and as the fluence increases, elementary C is formed as an adlayer on the top of the carbide. The same behaviour is also observed during MD simulations. Figure 10 illustrates a Be simulation cell bombarded with 1000 C ions with an impact energy of 20 eV. A few layers of $Be_2C$ are observed in the mixing region as well as amorphous C at the very top surface where the C concentration is high. The carbide is thus formed already on a picosecond time scale.

The carbon–beryllium system has also been studied from many other points of view. DFT calculations have suggested that beryllium carbide can form via Be diffusion into graphite, forming first an intercalated beryllium–carbon compound, which then undergoes a phase transition to beryllium carbide [213]. Sang *et al* have developed a multiscale particle-balance model for reaction–diffusion and
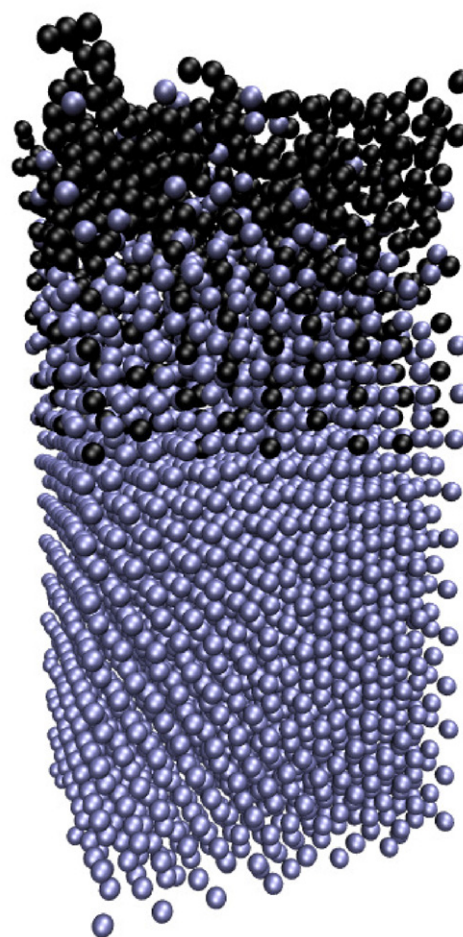


**Figure 10.** Structure of a Be cell bombarded with 20 eV C ions. $Be_2C$ layers are formed in the mixing region.

hydrogen inventory modelling in porous mixed Be–W–C layers [214]. Combinations of such different kinds of models will certainly lead to an increased understanding of mixed materials in fusion conditions.

### 4.2.1. Potentials for mixed materials.
The formation of areas of amorphous C on the surface of mixed BeC materials sets certain requirements on the interatomic potentials used to simulate sputtering by H isotopes from these materials. Incident ions with low kinetic energy have time to react chemically with surface atoms. While a Tersoff-type potential [121], originally developed for covalently bonded materials, can well be applied to mixed metallic-covalent systems [123] such as BeC, this potential does not capture the very particular chemical behaviour of hydrocarbon systems.

The Brenner potential, on the other hand, is developed specifically to model intramolecular chemical bonding in hydrocarbons [103]. Brenner used the functional form of the Tersoff potential as a starting point, and added terms to this which account for the forces that arise from the specific bonding behaviour of hydrocarbons.

Bond conjugation is seen in certain hydrocarbon systems when assigning single or double character to bonds which results in a chain of alternating single and double bonds
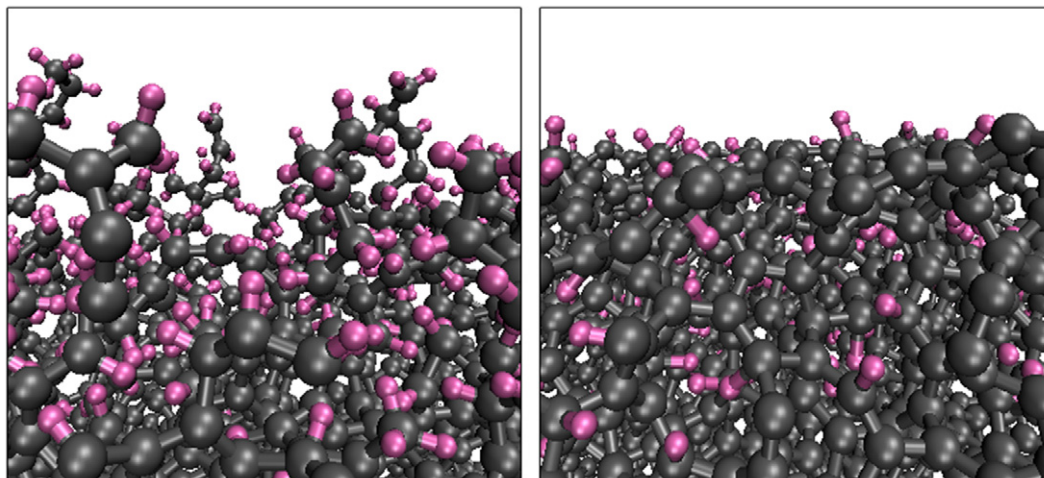
**Figure 11.** Amorphous C surfaces after 2000 consecutive D impacts. The picture to the right was simulated using a Tersoff-type potential, while to the left the Brenner hydrocarbon potential was used. Large (grey) spheres represent C atoms and smaller pink spheres represent D atoms. Adapted with permission from [217], Copyright 2013 Elsevier.

between C atoms, such as in aromatic rings and graphene. In these configurations the C–C bonds actually share single and double bond character, and all are in fact of equal strength. On the other hand, situations arise where the nearest neighbourhood of an atom pair is indistinguishable from the above configurations, yet neighbouring single and double bonds do not have shared character, but are in fact clearly double and single, respectively. This behaviour depends on the atoms that the neighbours to the pair in question are bonded to. Thus, in order to determine whether a bond should be purely single or double, or mixed, a potential must take into consideration a larger area around a given bond.

The occurrence of free radicals is another special case arising in hydrocarbon systems which is not described by a calculation of bond strength based only on immediate neighbours. In this case a C atom does not share all its bonding electrons between its neighbours, but rather retains a high degree of reactivity, while at the same time the existing bonds are weaker than they would be if all electrons were involved.

Brenner's hydrocarbon potential accounts for these particular chemical effects by including terms dependent on the number and nature of second neighbours (i.e. neighbours of neighbours) to the pair whose bond is being calculated. The effect in low-energy sputtering simulations is that carbon chains along the material surface more readily become hydrogenated, in comparison with the predictions of the pure Tersoff-type potential. This results in a substantial sputtering yield at low energies, which is consistent with experiment [215, 216]. The high yield is due to the formation of terminating methyl-like groups, which are the precursors to sputtered molecules [109]. Because of this the specific surface configuration of a sample has a large impact on the probability of chemical sputtering. Such terminating methyl groups are not formed in simulations with a Tersoff-type potential [217]. Figure 11 shows the difference in surface structure of an amorphous C surface after consecutive D bombardment with the two potentials.

*4.2.2. MD simulations of SCS in BeC.* Surface evolution during D irradiation, captured by cumulative bombardments, is important in the BeC system due to the strong dependence on the surface configuration of the sputtering of the C component. This is especially true when the surface contains sizeable areas of amorphous C. In order to realistically capture the surface evolution in this case, the above-mentioned chemical effects must be included. For this mixed metallic-covalent system, a viable solution utilizing current potentials is to simultaneously use both a Tersoff-type potential and the Brenner hydrocarbon potential. The calculation of a given bond then depends on which species are present among the atoms affecting the bond.

The analytical bond-order potential (ABOP) for the Be–C system [128] predicts the formation of areas of amorphous carbon and crystalline $Be_2C$, when a simulation cell containing excess C is annealed. In this way a realistic $Be_2C$ surface with an amorphous C area was created, and bombarded using the combined Be–C–D ABOP and Brenner potentials [217]. Comparison to simulations using only the Be–C–D ABOP show the importance of hydrocarbon chemical effects, especially when predicting the relative degree of sputtering of the different surface components. Simulations with the hybrid potential show a higher degree of C sputtering, and also the degree of molecular sputtering at lower energies was higher, as compared to yields obtained using the pure Tersoff-type potential. The sputtering yields for the two cases are shown in figure 12. For 10–50 eV ions chemical effects dominate, and C is sputtered preferentially over Be. Between 50 and 75 eV there is a turning point, when physical sputtering processes begin to dominate, so that above this the lighter element Be is sputtered preferentially, despite half of the simulated surface being composed of amorphous C.

## 5. To macroscopic time scales: H and He in W

### 5.1. H retention in W

The refractory metal tungsten (W) has extraordinary physical and thermal properties and is intended to be used as a
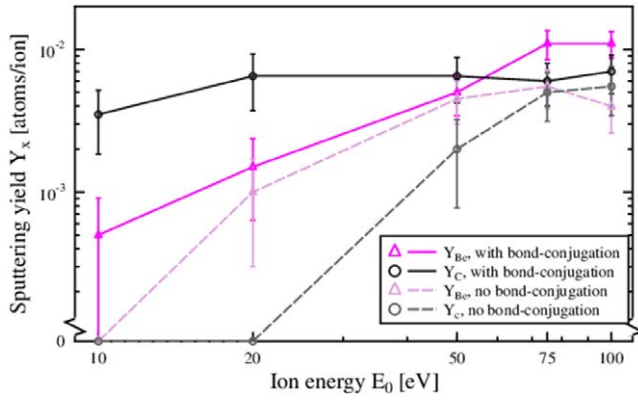
J. Phys. D: Appl. Phys. **47** (2014) 224018

K Nordlund *et al*

**Figure 12.** Sputtering yield from a mixed material surface with areas of Be$_2$C and amorphous C, simulated with and without the bond-conjugation terms in the Brenner potential. Adapted with permission from [217], Copyright 2013 Elsevier.
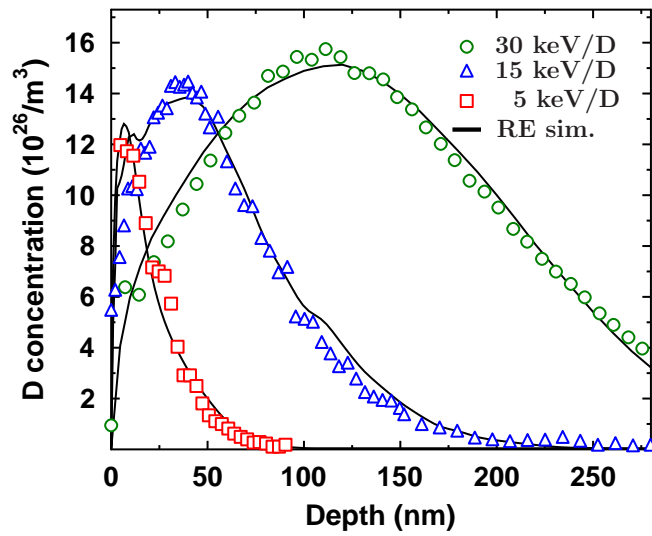


**Figure 13.** Experimental and simulated D distributions in W, with implantation energies of 5, 15 and 30 keV/D, to a fluence of $5.8 \times 10^{20}$ D/m$^2$.
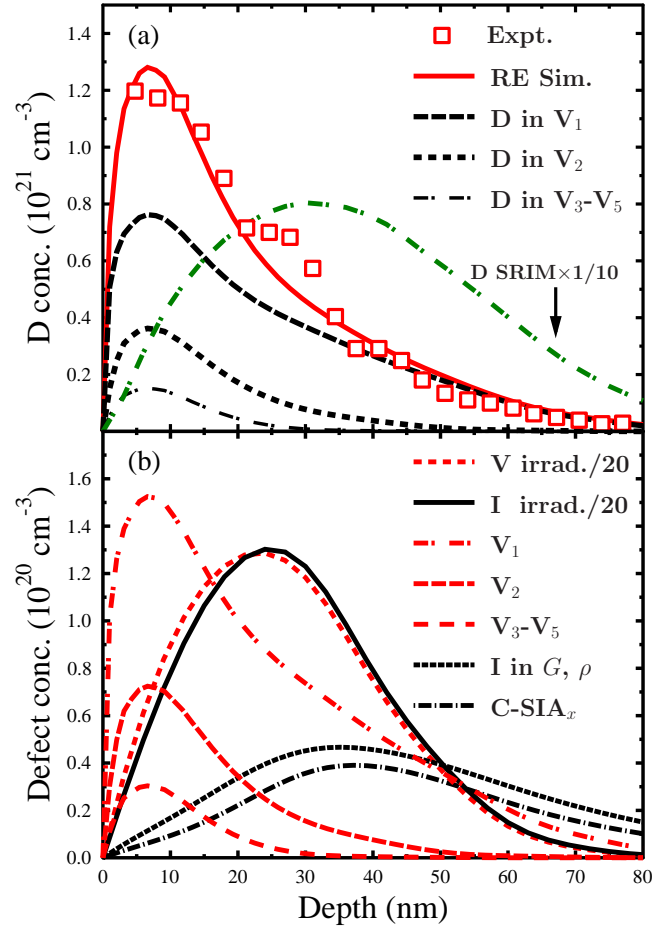


**Figure 14.** Data for the 5 keV/D implantation. (*a*) The total simulated D profile (solid line) consists mainly of D trapped in monovacancies, while the concentration of D trapped in larger vacancy clusters, decreases along with the cluster size. The SRIM simulation shows the D profile in the case where the implantation would have been done at a temperature where D is immobile (i.e. in the absence of the diffusion that is included in the rate equation (RE) simulations). (*b*) Implantation induced and final defect profiles. The remaining (about 5% of the initially produced) SIAs in the sample are in grain boundaries ($G$), dislocations ($\rho$) and in carbon impurity SIA$_x$ clusters. Reproduced with permission from [218], Copyright 2012 Elsevier.

plasma-facing component in the next ITER fusion device. As a first wall material in ITER, W will be subjected to both low-energy, high flux hydrogen (H) isotopes and high-energy neutrons that will create H trapping damage deep in the wall material. The H isotope retention should be kept as low as possible for both fusion efficiency and safety reasons. The natural and irradiation-induced traps will retain H isotopes and especially important is tritium (T) retention. To understand the H retention in W, RE simulations above the 5B displacement threshold energy $E_{th}$ are considered.

The simulated and experimental deuterium (D) retention in polycrystalline W at room temperature are compared. The D is implanted into W to a fluence of $5.8 \times 10^{20}$ D m$^{-2}$, with three different implantation energies, 5, 15 and 30 keV/D, with a flux of about $3.2 \times 10^{17}$ D m$^{-2}$s. The main impurity, excluding Mo, in the W samples was carbon (C) $\sim 10 \mu$g g$^{-1}$, corresponding to about $10^{25}$ C atoms m$^{-3}$ (typical high purity 99.99% polycrystalline W by Plansee AG). The experimental details are described in [218] and RE details in [219].

An excellent agreement between the RE simulated, and all the 5, 15 and 30 keV/D experimental D concentration profiles was found, see figure 13. The fraction of the retained D, compared to the implanted fluence of $5.8 \times 10^{20}$ D m$^{-2}$, increases rapidly from about 8% to 35% as the implantation energy increases from 5 to 30 keV/D.

The final simulation outcome after irradiation is presented for the 5 keV/D case in figure 14. The present RE simulation results give not only the total retained D, but the quantitative amounts of D trapped in each defect type. Of the total implanted D fluence $5.8 \times 10^{20}$ D m$^{-2}$, at 5 keV about 29% is directly backscattered, 63% diffuses to the surface and desorbs to vacuum, and only 8% is retained in the sample.

It was observed that at 5 keV, about 75% of the retained D is trapped in monovacancies and vacancy clusters, and the rest in impurities, grain boundaries and/or dislocations, extending deep into the sample, see figure 15. The maximum range
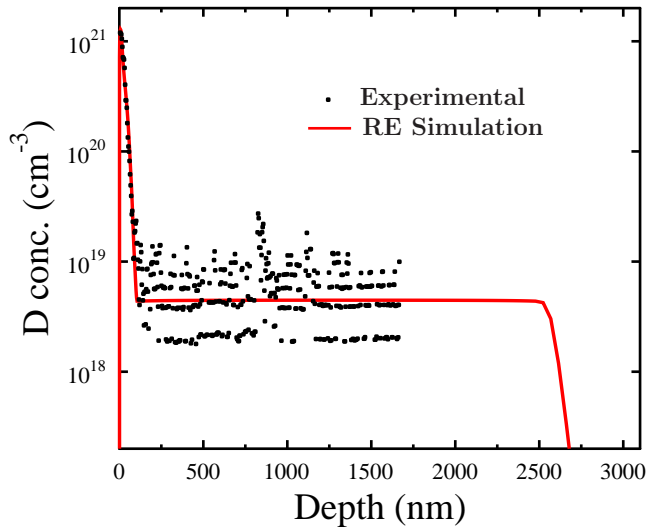
**Figure 15.** The experimental and simulated 5 keV/D profiles in logarithmic scale. The simulation was done by adding a D trapping impurity concentration of $4.5 \times 10^{15}$ cm$^{-3}$. Reproduced with permission from [218]. Copyright 2012 Elsevier.
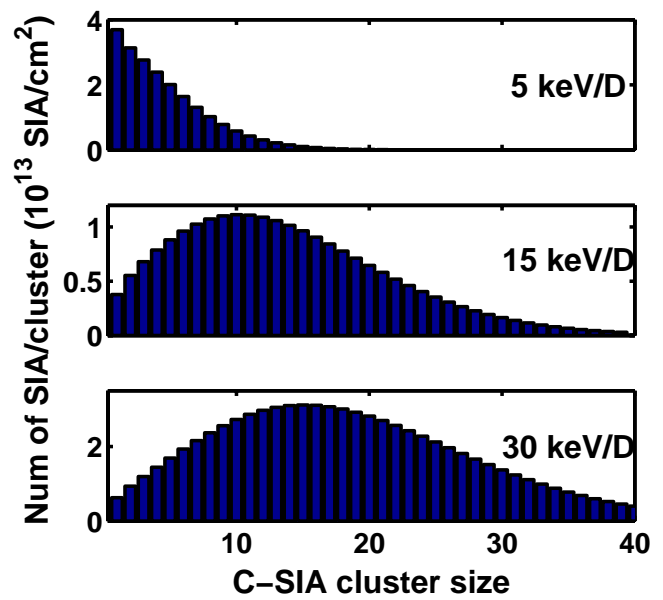


**Figure 16.** Number of different sized C-SIA clusters for increasing implantation energy. The mean number of SIAs per cluster is about 5 for 5 keV, 14 for 15 keV and 18 for 30 keV. Reproduced with permission from [218]. Copyright 2012 Elsevier.

for trapped D increases from about $2.6\,\mu$m at 5 keV, to about $4.5\,\mu$m at 30 keV. These deep extending D tails have also been observed in other experiments, for example by Alimov *et al* [220]. At higher fluences, the retained fraction deep in the sample, will eventually be much larger than the fraction close to the surface, which will be especially important for tritium retention. The nature of these deep extending traps is not clear, however. They have been observed in both polycrystalline and single crystal material, with the mean trapped D amount being higher in coarse grained, than in single crystal W [220], indicating that part of these D traps could be grain boundaries. The binding of D atoms to the grain boundary has been studied by Zhou *et al* using DFT [221]. Their result suggests a binding energy between 0.8 and 1.5 eV, which certainly would trap D at room temperature.

The present samples are not coarse grained, and the number of trapping sites at grain boundaries, should not alone be sufficient to account for the experimental value of about $5 \times 10^{24}$ m$^{-3}$. A dislocation density of about $10^{14}$ m$^{-2}$, is also too low to explain the traps. Another additional alternative is that D is trapped in impurities. One potential trapping impurity present in the sample is oxygen ($5\,\mu$g g$^{-1}$). Haasz *et al* noticed that the D and O depth profiles were quite similar in single crystal W [222]. This finding is a strong indication that O binds D, and DFT calculations are underway to confirm this and to give a value for the binding energy.

Figure 14(*b*) shows the irradiation-induced and the final defect profiles. The irradiation-induced profiles are the sum of self-interstitial atom (SIA) and vacancy profiles times the implanted fluence. The total number of irradiation-induced vacancies and SIAs per incoming D is 0.16 at 5 keV, 0.79 at 15 keV and 1.6 at 30 keV. About 93–96% of these vacancies are annihilated by the diffusing SIAs during the irradiation. The remaining SIAs in the sample have been trapped by dislocations and grain boundaries and C-SIA$_x$ clusters, where $x$ is the number of SIAs in the cluster. The size distributions

of the C-SIA$_x$ clusters are shown in figure 16, where the total integrated amount of SIAs in these clusters increases from about $2.1 \times 10^{18}$ m$^{-2}$ for 5 keV to about $8.1 \times 10^{18}$ m$^{-2}$ for 30 keV implantation. Also, the average cluster size is seen to increase, as more SIAs are produced at higher D implantation energies. These C-SIA$_x$ clusters could be the experimentally observed interstitial type dislocation loops [223].

The flux of D, and the corresponding SIA production rate, is too small for producing large SIA or D-SIA clusters. Large SIA clusters were only observed if it was assumed that there is an impurity that initially forms a bound complex with an SIA. This complex then serves as a nucleation site for large impurity–SIA clusters. If the SIA production rate is large enough, large SIA clusters can form without the need of impurities. Further evidence for the formation of impurity–SIA complexes is given by the 8 keV H irradiation experiment by Sakamoto *et al* [224], which shows that the interstitial dislocation loop areal density increases when the impurity concentration increases.

A remarkable observation is that the final retained D profile, figure 14(*a*), resembles neither the implanted D, nor the irradiation-induced vacancy profile figure 14(*b*). During the D-induced collision cascades, the vacancies are produced on average a bit closer to the surface than the SIAs. The SIA-vacancy annihilation is proportional to both their respective concentrations, resulting in vacancies deeper than about 30 nm being effectively annihilated, and therefore, the remaining vacancy profile is shifted towards the surface. Hence, any short time and D fluence simulation method trying to produce the observed retained D profile will fail, because the vacancy, and in the vacancies trapped D profiles will shift more and more towards the surface with increasing D fluence.

Figure 17(*a*) shows the time evolution of the retained D during, and shortly after the 30 keV/D room temperature
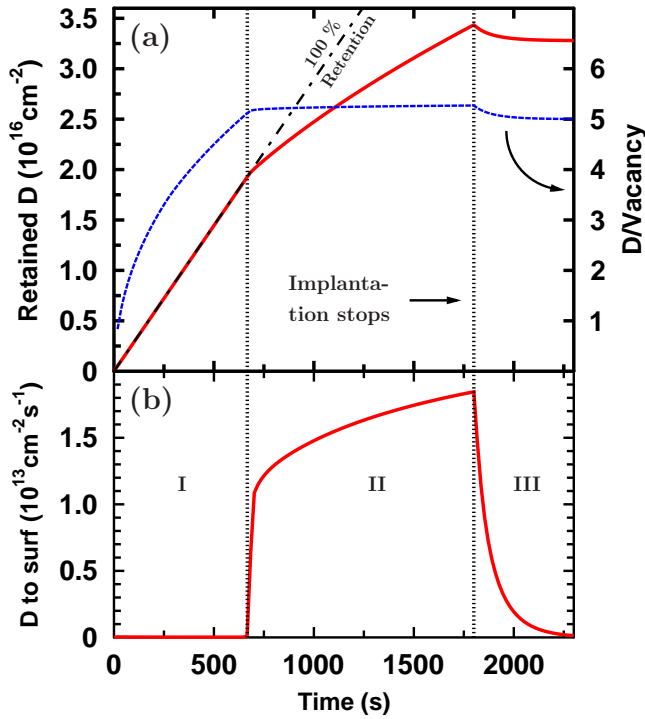
J. Phys. D: Appl. Phys. **47** (2014) 224018

K Nordlund *et al*



**Figure 17.** (*a*) Retained D and the mean number of D trapped per vacancy, during and after 30 keV/D room temperature implantation. (*b*) The flux of D atoms from bulk to sample surface. Region I: vacancies are slowly filling up with D, 100% retention. Region II: vacancies are saturated with D, and D flux to surface starts. Region III: weakly bound sixth D detraps from vacancies after the implantation. Reproduced with permission from [218]. Copyright 2012 Elsevier.

implantation. In the figure, three distinct regions are elucidated. In region I, the retained D is the same as the implanted one (100% retention, backscattered fraction excluded).

In region II, the vacancies become saturated with D, and the mean number of trapped D per vacancy, is between five and six. All the implanted D atoms are no longer trapped, but diffuse deeper into the sample, and to the sample surface. In figure 17(*b*) is shown the simultaneous onset of D atom flux to the W surface. After the implantation has stopped (region III), the D retention drops and a remnant D flux to the W surface takes place for about 10 min. The simulation results show that the slow decrease in the retained D, is the detrapping of the sixth D from monovacancies (trapping energy 0.61 eV). This post implantation effect has been seen experimentally for example by García-Rosales *et al* [225] and Pisarev *et al* [226] where the observed $D_2$ desorption from the sample surface, resembles the present simulated D flux to the surface in figure 17(*b*).

### 5.2. He bubble and fuzz formation in W

Recent experiments [48] have shown that He bombardment of W can lead to the formation of a highly underdense fuzz-like morphology under fusion relevant conditions [227], such as substrate temperatures of 1000–2000 K [228], low irradiation energies ($\leqslant$30 eV) [229] and He fluxes of $10^{20}$–$10^{23}$ m$^{-2}$ s$^{-1}$ [230]. However, the underlying
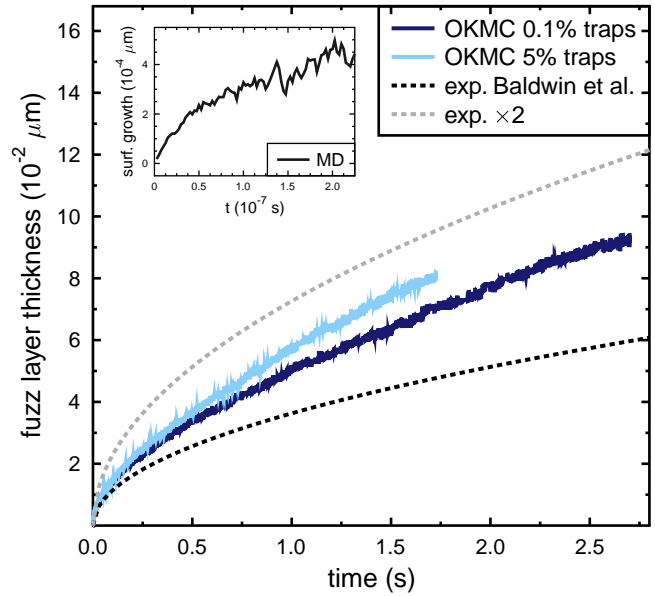


**Figure 18.** The fuzz layer thickness growth as a function of time. The OKMC results (thick lines) were obtained using the parameters taken from [48], for different defect concentrations. The experimental growth rate (exp) is interpolated from the results in [48]. The upper boundary exp.2 is calculated as double that of exp, accounting for factors such as the W-grade [235]. The surface growth in MD [195] is shown for a comparison, plotted separately as the time scales differ by seven orders of magnitude. Figure reproduced with permission from [233]. Copyright 2014 EPLA.

mechanisms remain unclear. Some theoretical models explain the phenomena qualitatively, for instance based on W viscoelasticity [231], stress-driven bubble growth [232] or adatom diffusion [233]. As a step forward, Lasa *et al* [234] developed a multiscale model where insights from MD simulations on He bubble development was used to parameterize a KMC model on the bubble and surface growth. The model is based on the balance between the surface growth due to the He bubble formation and consequent dislocation loop punching and the drop by bubble blistering, leading to a stochastic surface evolution that explains the square root of time dependence and gives quantitative agreement with experiments (see figure 18). However, no model has addressed yet key issues such as the upper and lower temperature thresholds for the fuzz formation or the growth rate saturation with increasing flux.

Further, the general interaction of He with the pre-existing defects in (bulk) W, including the damage caused by energetic $\alpha$ (He) particles, is gaining relevance in plasma–wall interaction studies. For example, a detailed multiscale model was developed by Becquart *et al*, combining the DFT [236–238] and KMC [239] methods, to explain the dynamics of He and point defects in W.

## 6. Summary

In this review article, we have given an overview of the physics and chemistry of plasma–wall interactions in tokamak-like fusion reactors, and presented some of the most commonly used material simulation approaches used to study them. We

J. Phys. D: Appl. Phys. **47** (2014) 224018

K Nordlund *et al*

have described the swift chemical sputtering mechanism, and shown how it can explain the erosion of molecular species from both carbon- and beryllium-based first wall materials. We have further discussed the atom-level mechanisms of mixed material formation of the reactors, and how binding chemistry affects their sputtering. Finally we have shown how rate equations, parametrized from lower level simulation methods in a multiscale scheme, can be used to describe the hydrogen isotope diffusion and retention in tungsten-based fusion reactor divertors.

## Acknowledgments

## References

[1] Wesson J 1997 *Tokamaks* 2nd edn (*Oxford Engineering Series* No 48) (Oxford: Clarendon)

[2] ITER Physics Basis Editors, ITER Physics Expert Group Chairs and Co-Chairs and ITER Joint Central Team and Physics Integration Unit 1999 ITER physics basis *Nucl. Fusion* **39** 2137–638

[3] Baonian W 2007 Physical engineering test and first divertor plasma configuration in east *Plasma Sci. Technol.* **9** 125

[4] Kurki-Suonio T, Hynönen V, Ahlgren T, Nordlund K, Sugiyama K, Dux R and the ASDEX Upgrade Team 4 2007 Fusion tritons and plasma-facing components in a fusion reactor *Europhys. Lett.* **78** 65002

[5] Victoria M *et al* 2007 Modeling irradiation effects in fusion materials *Fusion Eng. Des.* **82** 2413–21

[6] Dudarev S L *et al* 2009 The EU programme for modelling radiation effects in fusion reactor materials: an overview of recent advances and future goals *J. Nucl. Mater.* **386–8** 1–7

[7] Grove W R 1852 On the electro-chemical polarity of gases *Phil. Trans. R. Soc. Lond.* **142** 87

[8] Bohr N 1913 On the theory of the decrease of velocity of moving electrified particles on passing through matter *Phil. Mag.* **25** 10

[9] Rutherford E 1911 The scattering of $\alpha$ and $\beta$ rays by matter and the structure of the atom *Phil. Mag.* **6** 31

[10] Leavitt J A, McIntyre L C Jr and Weller M R 1995 *Backscattering Spectrometry* (Pittsburgh, PA: Materials Research Society)

[11] Feldman L C and Mayer J W 1986 *Fundamentals of Surface and Thin Film Analysis* (New York: North-Holland)

[12] Hochman R F (ed) 1986 *Ion Plating and Implantation. Applications to Materials* (Materials Park, OH: American Society for Metals)

[13] Harper J M E, Cuomo J J and Hentzell H T G 1985 Synthesis of compound thin films by dual ion beam deposition: I. Experimental approach *J. Appl. Phys.* **58** 550–5

[14] Brown W L, Jarrold M F, McEachern R L, Sosnowski M, Usui H, Takaoka G and Yamada I 1991 Ion cluster beam deposition of thin films *Nucl. Instrum. Methods Phys. Res.* B **59–60** 182–9

[15] Mayer J W and Lau S S 1990 *Electronic Materials Science For Integrated Circuits in Si and GaAs* (New York: MacMillan)

[16] Nastasi M, Mayer J and Hirvonen J 1996 *Ion–Solid Interactions—Fundamentals and Applications* (Cambridge: Cambridge University Press)

[17] Krasheninnikov A V and Nordlund K 2010 Ion and electron irradiation-induced effects in nanostructured materials *J. Appl. Phys.* **107** 071301

[18] Merola M 2013 *Public Presentation at the 16th Int. Conf. on Fusion Reactor Materials (Beijing, China, 21 October 2013)*

[19] Brinkman J A 1954 On the nature of radiation damage in metals *J. Appl. Phys.* **25** 961

[20] Diaz de la Rubia T, Averback R S, Benedek R and King W E 1987 Role of thermal spikes in energetic collision cascades *Phys. Rev. Lett.* **59** 1930–3
   Diaz de la Rubia T, Averback R S, Benedek R and King W E 1988 *Phys. Rev. Lett.* **60** 76 (erratum)

[21] Averback R S and Diaz de la Rubia T 1998 Displacement damage in irradiated metals and semiconductors *Solid State Physics* vol 51 ed H Ehrenfest and F Spaepen (New York: Academic) pp 281–402

[22] Diaz de la Rubia T and Guinan M W 1991 New mechanism of defect production in metals: a molecular-dynamics study of interstitial-dislocation-loop formation at high-energy displacement cascades *Phys. Rev. Lett.* **66** 2766

[23] Ghaly M, Nordlund K and Averback R S 1999 Molecular dynamics investigations of surface damage produced by keV self-bombardment of solids *Phil. Mag.* A **79** 795

[24] Nordlund K, Tarus J, Keinonen J, Donnelly S E and Birtcher R C 2003 Atomic fingers, bridges and slingshots: formation of exotic surface structures during ion irradiation of heavy metals *Nucl. Instrum. Methods Phys. Res.* B **206** 189–93

[25] Behrisch R (ed) 1981 *Sputtering by Particle Bombardment I* (Berlin: Springer)

[26] Sigmund P 1993 Introduction to sputtering *Mat.-Fys. Medd. K. Dan. Vidensk. Selsk.* **43** 7–26

[27] Merkle K L and Jäger W 1981 Direct observation of spike effects in heavy-ion sputtering *Phil. Mag.* A **44** 741

[28] Ghaly M and Averback R S 1994 Effect of viscous flow on ion damage near solid surfaces *Phys. Rev. Lett.* **72** 364–7

[29] Townsend P D 1986 Ion implantation—an introduction *Contemp. Phys.* **27** 241

[30] Kirk M A, Robertson I M, Jenkins M L, English C A, Black T J and Vetrano J S 1987 The collapse of defect cascades to dislocation loops *J. Nucl. Mater.* **149** 21

[31] Zinkle S J 1999 Fundamental radiation effects parameters in metals and ceramics *Radiat. Eff. Defects Solids* **148** 447–77

[32] Kiritani M, Yoshiie T and Kojima S 1986 Factors controlling the nature and amount of residual defects in neutron irradiated metals *J. Nucl. Mater.* **141–3** 625–32

[33] Kojima S, Satoh Y, Taoka H, Ishida I, Yoshie T and Kiritani M 1989 Confirmation of vacancy-type stacking fault tetrahedra in quenched, deformed and irradiated face-centred cubic metals *Phil. Mag.* A **59** 519–32

[34] Nordlund K and Gao F 1999 Formation of stacking fault tetrahedra in collision cascades *Appl. Phys. Lett.* **74** 2720–2

[35] Ruault M O, Chaumont J, Penisson J M and Bourret A 1984 High resolution and *in situ* investigation of defects in bi-irradiated Si *Phil. Mag.* A **50** 667

[36] Diaz de la Rubia T and Gilmer G H 1995 Structural transformations and defect production in ion implanted

silicon: a molecular dynamics simulation study *Phys. Rev. Lett.* **74** 2507–10

[37] Norris S A, Samela J, Madi C S, Brenner M P, Bukonte L, Backman M, Djurabekova F, Nordlund K and Aziz M J 2011 MD-predicted phase diagrams for pattern formation *Nature Commun.* **2** 276

[38] Dhara S 2007 Formation, dynamics, and characterization of nanostructures by ion beam irradiation *Crit. Rev. Solid State Mater. Sci.* **32** 1–50

[39] Salh R, Fitting L, Kolesnikova E V, Sitnikova A A, Zamoryanskaya M V, Schmidt B and Fitting H J 2007 Si and Ge nanocluster formation in silica matrix *Semiconductors* **41** 381

[40] Donnelly S E, Birtcher R C, Templier C and Vishnyakov V 1995 Response of helium bubbles in gold to displacement-cascade damage *Phys. Rev. B* **52** 3970

[41] Birtcher R C, Donnelly S E, Song M, Furuya K, Mitsuishi K and Allen C W 1999 Behavior of crystalline Xe nanoprecipitates during coalescence *Phys. Rev. Lett.* **83** 1617

[42] Condon J B and Schober T 1993 Hydrogen bubbles in metals *J. Nucl. Mater.* **207** 1–24

[43] Mayer J W 1971 Ion implantation-lattice disorder *Radiation Effects in Semiconductors* ed J W Corbett and G D Watkins (Londan: Gordon and Breach) p 367

[44] Nordlund K, Keinonen J, Rauhala E and Ahlgren T 1995 Range profile in self-ion-implanted crystalline Si *Phys. Rev. B* **52** 15170

[45] Chason E *et al* 1997 Ion beams in silicon processing and characterization *J. Appl. Phys.* **81** 6513–61

[46] Pelaz L, Marqués L A, Aboy M, Barbolla J and Gilmer G H 2003 Atomistic modeling of amorphization and recrystallization in silicon *Appl. Phys. Lett.* **82** 2038

[47] Stritzker B, Elliman R G and Zou J 2000 Self-ion-induced swelling of germanium *Nucl. Instrum. Methods Phys. Res. B* **175** 193

[48] Baldwin M J and Doerner R P 2008 Helium induced nanoscopic morphology on tungsten under fusion relevant plasma conditions *Nucl. Fusion* **48** 035001

[49] Kajita S, Yoshida N, Yoshihara R, Ohno N and Yamagiwa M 2011 TEM observation of the growth process of helium nanobubbles on tungsten: nanostructure formation mechanism *J. Nucl. Mater.* **418** 152–8

[50] Loarte A 2004 Implications of the use of carbon-based plasma facing components in next step fusion devices *Phys. Scr.* **T111** 13–22

[51] Wang W, Roth J, Lindig S and Wu C H 2001 Blister formation of tungsten due to ion bombardment *J. Nucl. Mater.* **299** 124

[52] Nishikawa M 1998 High flux dependence of erosion and retention in beam experiments and its significance to fusion systems *Fusion Eng. Des.* **41** 47–53

[53] Lipschultz B *et al* 2010 An assessment of the current data affecting tritium retention and its use to project towards *t* retention in ITER *Technical Report* PSFC/RR-10-4, MIT

[54] Küppers J 1995 The hydrogen surface chemistry of carbon as a plasma facing material *Surf. Sci. Rep.* **22** 249–321

[55] Robinson M T and Torrens I M 1974 Computer simulation of atomic-displacement cascades in solids in the binary-collision approximation *Phys. Rev. B* **9** 5008

[56] Snoeks E, Polman A and Volkert C A 1994 Densification, anisotropic deformation, and plastic flow of SiO$_2$ during MeV heavy ion irradiation *Appl. Phys. Lett.* **65** 2487

[57] Jones R O and Gunnarsson O 1989 *Rev. Mod. Phys.* **61** 689

[58] For a review, see Jones R O and Gunnarsson O 1989 *Rev. Mod. Phys.* **61** 689

[59] Uhlmann S, Frauenheim Th, Boyd K J, Marton D and Rabalais J W 1997 Elementary processes during low-energy self-bombardment of Si(1 0 0) 2 × 2—a molecular dynamics study *Radiat. Eff. Defects Solids* **141** 185

[60] Krasheninnikov A V, Nordlund K, Salonen E, Keinonen J and Wu C H 2002 Sputtering of amorphous hydrogenated carbon by hyperthermal ions as studied by tight-binding molecular dynamics *Comput. Mater. Sci.* **25** 427–34

[61] Holmström E, Kuronen A and Nordlund K 2008 Threshold defect production in silicon determined by density functional theory molecular dynamics simulations *Phys. Rev. B* **78** 045202

[62] Korhonen T, Puska M J and Nieminen R M 1996 Vacancy formation energies for fcc and bcc transition metals *Phys. Rev. B* **51** 9526

[63] Carling K, Wahnström G, Mattsson T R, Sandberg N and Grimvall G 2003 Vacancy concentration in al from combined first-principles and model potential calculations *Phys. Rev. B* **67** 054101

[64] Fu C-C, Willaime F and Ordejon P 2004 Stability and mobility of mono- and di-interstitials in α-Fe *Phys. Rev. Lett.* **92** 175503–1

[65] Korzhavyi P A, Ruban A V, Lozovoi A Y, Vekilov Yu Kh, Abrikosov I A and Johansson B 2000 Constitutional and thermal point defects in B$_2$ NiAl *Phys. Rev. B* **61** 6003

[66] Mishin Y, Lozovoi A Y and Alavi A 2003 Evaluation of diffusion mechanisms in NiAl by embedded-atom and first-principles calculations *Phys. Rev. B* **67** 014201

[67] Olsson P, Abrikosov I A, Vitos L and Wallenius J 2003 *Ab initio* formation energies of Fe–Cr alloys *J. Nucl. Mater.* **321** 84

[68] Puska M J, Pöykkö S, Pesola M and Nieminen R M 1998 Convergence of supercell calculations for point defects in semiconductors: vacancy in silicon *Phys. Rev. B* **58** 1318–25

[69] Mattila T and Nieminen R M 1995 Direct antisite formation in electron irradiation of gaas *Phys. Rev. Lett.* **74** 2721

[70] Erhart P, Albe K and Klein A 2006 First-principles study of intrinsic point defects in ZnO: role of band structure, volume relaxation and finite size effects *Phys. Rev. B* **73** 205203

[71] Janotti A and Van de Walle C G 2007 Native point defects in ZnO *Phys. Rev. B* **76** 165202

[72] Gupta F, Brillant G and Pasturel A 2007 Correlation effects and energetics of point defects in uranium dioxide: a first principle investigation *Phil. Mag.* **87** 2561–9

[73] Robinson M T and Oen O S 1963 The channeling of energetic atoms in crystal lattices *Appl. Phys. Lett.* **2** 30

[74] Smith R (ed) 1997 *Atomic and Ion Collisions in Solids and at Surfaces: Theory, Simulation and Applications* (Cambridge: Cambridge University Prss)

[75] Ziegler J F, Biersack J P and Littmark U 1985 *The Stopping and Range of Ions in Matter* (New York: Pergamon)

[76] Ziegler J F 2013 SRIM-2013 software package, available online at www.srim.org

[77] Ziegler J F, Biersack J P and Ziegler M D 2008 *SRIM—The Stopping and Range of Ions in Matter* (Chester, MD: SRIM)

[78] Möller W and Eckstein W 1984 Tridyn—a trim simulation code including dynamic composition changes *Nucl. Instrum. Methods Phys. Res. B* **2** 814

[79] Pugacheva T S, Djurabekova F G and Valiev S Kh 1998 Effects of cascade mixing, sputtering and diffusion by high dose light ion irradiation of boron nitride *Nucl. Instrum. Methods Phys. Res. B* **141** 99–104

[80] Robinson M T 1992 Computer simulation studies of high-energy collision cascades *Nucl. Instrum. Methods Phys. Res. B* **67** 396

[81] Posselt M and Biersack J P 1992 Computer-simulation of ion-implantation into crystalline targets *Nucl. Instrum. Methods Phys. Res.* B **64** 706

[82] Stoller R E, Toloczko M B, Was G S, Certain A G, Dwaraknath S and Garner F A 2013 On the use of srim for computing radiation damage exposure *Nucl. Instrum. Methods Phys. Res.* B **310** 75

[83] Likonen J and Hautala M 1989 Binary collision lattice simulation study of model parameters in monocrystalline sputtering *J. Phys.: Condens. Matter* **1** 4697

[84] Henriksson K O E, Vörtler K, Dreißigacker S, Nordlund K and Keinonen J 2006 Sticking of atomic hydrogen on the tungsten (0 0 1) surface *Surf. Sci.* **600** 3167–74

[85] Möller W 1986 A computer study of the collisional mixing of Pt in Si *Nucl. Instrum. Methods Phys. Res.* B **15** 688

[86] Mayer M and Eckstein W 1994 Monte Carlo calculations of hydrogen and deuterium range distributions in light target materials *Nucl. Instrum. Methods Phys. Res.* B **94** 22

[87] Vichev R G and Karpuzov D S 1993 Time evolution of ion slowing-down in amorphous solids *Nucl. Instrum. Methods Phys. Res.* B **83** 345

[88] Gärtner K *et al* 1995 Round robin computer simulation of ion transmission through crystalline layers *Nucl. Instrum. Methods Phys. Res.* B **102** 183

[89] Hobler G and Kovac D 2011 Dynamic binary collision simulation of focused ion beam milling of deep trenches *Nucl. Instrum. Methods Phys. Res.* B **269** 1609

[90] Bukonte L, Djurabekova F, Samela J, Nordlund K, Norris S A and Aziz M J 2013 Comparison of molecular dynamics and binary collision approximation simulations for atom displacement analysis *Nucl. Instrum. Methods Phys. Res.* B **297** 23–8

[91] Lasa A, Schmid K and Nordlund K 2014 Modelling of W–Be mixed material sputtering under H irradiation *J. Nucl. Mater.* submitted

[92] Kirschner A, Philipps V, Winter J and Kögler U 2000 Simulation of the plasma–wall interaction in a tokamak with the Monte Carlo code ERO-TEXTOR *Nucl. Fusion* **40** 989

[93] Plank H, Wang W, Eckstein W, Schwörer R, Steffen H J and Roth J 1995 Deposition and hydrogen content of carbon films grown by $CH_3^+$ ion-beam bombardment *J. Appl. Phys.* **78** 5366

[94] Plank H and Eckstein W 1997 Preferential sputtering of carbides under deuterium irradiation—a comparison between experiment and computer simulation *Nucl. Instrum. Methods Phys. Res.* B **124** 23–30

[95] Eckstein W, Dohmen R, Mutzke A and Schneider R SDTrimSP: a Monte-Carlo code for calculating collision phenomena in randomized targets http://edoc.mpg.de/287291

[96] Allen M P and Tildesley D J 1989 *Computer Simulation of Liquids* (Oxford: Oxford University Press)

[97] Lesar R 2013 *Introduction to Computational Materials Science* (Cambridge: Cambridge University Press)

[98] Leach A R 2001 *Molecular Modelling: Principles and Applications* 2nd edn (Harlow: Pearson Education)

[99] Frenkel D and Smit B 2002 *Understanding Molecular Simulation: from Algorithms to Applications* 2nd edn (San Diego, CA: Academic)

[100] Nordlund K 1995 Molecular dynamics simulation of ion ranges in the 1–100 keV energy range *Comput. Mater. Sci.* **3** 448

[101] Nordlund K, Ghaly M, Averback R S, Caturla M, Diaz de la Rubia T and Tarus J 1998 Defect production in collision cascades in elemental semiconductors and fcc metals *Phys. Rev.* B **57** 7556–70

[102] Zarkadoula E, Dove M T, Trachenko K, Daraszewicz S L, Duffy D M, Seaton M, Todorov I T and Nordlund K 2013 The nature of high-energy radiation damage in iron *J. Phys. Condens. Matter.* **25** 125402

[103] Brenner D W 1990 Empirical potential for hydrocarbons for use in simulating the chemical vapor deposition of diamond films *Phys. Rev.* B **42** 9458
Brenner D W 1992 *Phys. Rev.* B **46** 1948

[104] Brenner D W, Shenderova O A, Harrison J A, Stuart S J and Sinnott S B 2002 A second-generation reactive empirical bond order (REBO) potential energy expression for hydrocarbons *J. Phys.: Condens. Matter* **14** 783–802

[105] Stuart S J, Tutein A B and Harrison J A 2000 A reactive potential for hydrocarbons with intermolecular interactions *J. Chem. Phys.* **112** 6472

[106] van Duin A C T, Dasgupta S, Lorant F and Goddard W A III 2001 Reaxff: a reactive force field for hydrocarbons *J. Phys. Chem.* A **105** 9396

[107] Salonen E, Nordlund K, Tarus J, Ahlgren T, Keinonen J and Wu C H 1999 Suppression of carbon erosion by hydrogen shielding during high-flux hydrogen bombardment *Phys. Rev.* B **60** 14005

[108] Salonen E, Nordlund K, Keinonen J and Wu C H 2000 Bond-breaking mechanism of sputtering *Europhys. Lett.* **52** 504–10

[109] Salonen E, Nordlund K, Keinonen J and Wu C H 2001 Swift chemical sputtering of amorphous hydrogenated carbon *Phys. Rev.* B **63** 195415

[110] Salonen E 2004 Overview of the atomistic modeling of the chemical erosion of carbon *Phys. Scr.* **T111** 133–7

[111] Alman D A and Ruzic D N 2003 Molecular dynamics calculation of carbon/hydrocarbon reflection coefficients on a hydrogenated graphite surface *J. Nucl. Mater.* **313–16** 182–6

[112] Marian J, Zepeda-Ruiz L A, Couto N, Bringa E M, Gilmer G H, Stangeby P C and Rognlien T D 2007 *J. Appl. Phys.* **101** 044506

[113] Krstic P S, Reinhold C O and Stuart S 2007 Chemical sputtering from amorphous carbon under bombardment by deuterium atoms and molecules *New J. Phys.* **9** 209

[114] Krstic P S, Reinhold C O and Stuart S 2007 Chemical sputtering by impact of excited molecules *Europhys. Lett.* **77** 33002

[115] Maya P N, von Toussaint U and Hopf C 2008 Synergistic erosion process of hydrocarbon films: a molecular dynamics study *New J. Phys.* **10** 023002

[116] Finnis M W and Sinclair J E 1984 A simple empirical n-body potential for transition metals *Phil. Mag.* A **50** 45
Finnis M W and Sinclair J E 1986 *Phil. Mag.* **53** 161 (erratum)

[117] Daw M S, Foiles S M and Baskes M I 1993 The embedded-atom method: a review of theory and applications *Mater. Sci. Rep.* **9** 251

[118] Kelchner C L, Halstead D M, Perkins L S, Wallace N M and DePristo A E 1994 Construction and evaluation of embedding functions *Surf. Sci.* **310** 425–35 and references therein

[119] Cleri F and Rosato V 1993 Tight-binding potentials for transition metals and alloys *Phys. Rev.* B **48** 22

[120] Dudarev S L and Derlet P M 2005 A magnetic interatomic potential for molecular dynamics simulations *J. Phys.: Condens. Matter* **17** 1–22

[121] Tersoff J 1988 New empirical approach for the structure and energy of covalent systems *Phys. Rev.* B **37** 6991

[122] Albe K, Nordlund K, Nord J and Kuronen A 2002 Modelling of compound semiconductors: analytical bond-order potential for Ga, As and GaAs *Phys. Rev.* B **66** 035205

[123] Albe K, Nordlund K and Averback R S 2002 Modeling metal-semiconductor interaction: analytical bond-order potential for platinum–carbon *Phys. Rev.* B **65** 195124

J. Phys. D: Appl. Phys. **47** (2014) 224018

K Nordlund *et al*

[124] Erhart P, Juslin N, Goy O, Nordlund K, Muller R and Albe K 2006 Analytic bond-order potential for atomistic simulations of zinc oxide *J. Phys.: Condens. Matter* **18** 6585–605

[125] Nord J, Albe K, Erhart P and Nordlund K 2003 Modelling of compound semiconductors: analytical bond-order potential for gallium, nitrogen and gallium nitride *J. Phys.: Condens. Matter* **15** 5649–62

[126] Juslin N, Erhart P, Träskelin P, Nord J, Henriksson K O E, Nordlund K, Salonen E and Albe K 2005 Analytical interatomic potential for modelling non-equilibrium processes in the W–C–H system *J. Appl. Phys.* **98** 123520

[127] Henriksson K O E and Nordlund K 2009 Simulations of cementite: an analytical potential for the Fe–C system *Phys. Rev.* B **79** 144107

[128] Björkas C, Juslin N, Timkó H, Vörtler K, Nordlund K, Henriksson K O E and Erhart P 2009 Interatomic potentials for the beryllium Be–C–H system *J. Phys.: Condens. Matter* **21** 445002

[129] Björkas C, Henriksson K O E, Probst M and Nordlund K 2010 A Be–W interatomic potential *J. Phys.: Condens. Matter* **22** 352206

[130] Ahlgren T, Heinola K, Juslin N and Kuronen A 2010 Bond-order potential for point and extended defect simulations in tungsten *J. Appl. Phys.* **107** 033516

[131] Li X-C, Shu X, Liu Y-N, Gao F and Lu G-H 2011 Modified analytical interatomic potential for a W–H system with defects *J. Nucl. Mater.* **408** 12–7

[132] Voter A F and Sorensen M R 1999 Accelerating atomistic simulations of defect dynamics: hyperdynamics, parallel replica dynamics, and temperature-accelerated dynamics *Multiscale Modelling of Materials* (*MRS Symp. Proc.* vol 538) ed V V Bulatov *et al* (Pittsburgh, PA: Materials Research Society) p 427

[133] Voter A F, Montalenti F and Germann T C 2002 Extending the time scale in atomistic simulation of materials *Annu. Rev. Mater. Res.* **32** 321–46

[134] Blackwell S, Smith R, Kenny S D and Walls J M 2012 Modeling evaporation, ion-beam assist, and magnetron sputtering of thin metal films over realistic time scales *Phys. Rev.* B **86** 035416

[135] Young W M and Elcock E W 1966 Monte Carlo studies of vacancy migration in binary ordered alloys: I *Proc. Phys. Soc.* **89** 735–46

[136] Bortz A B, Kalos M H and Lebowitz J L 1975 A new algorithm for Monte Carlo simulation of Ising spin systems *J. Comput. Phys.* **17** 10–8

[137] Fichthorn K A and Weinberg W H 1991 Theoretical foundations of dynamical Monte Carlo simulations *J. Chem. Phys.* **95** 1090

[138] Kotakoski J, Krasheninnikov A V and Nordlund K 2007 Kinetic Monte Carlo simulations of the response of carbon nanotubes to electron irradiation *J. Comput. Theor. Nanosci.* **4** 1153–9

[139] Djurabekova F G, Malerba L, Domain C and Becquart C S 2007 Stability and mobility of small vacancy and copper-vacancy clusters in Bcc–Fe: an atomistic kinetic Monte Carlo study *Nucl. Instrum. Methods Phys. Res.* B **255** 47–51

[140] Pelaz L, Marqués L A and Barbolla J 2004 Ion-beam-induced amorphization and recrystallization in silicon *J. Appl. Phys.* **96** 5947–76

[141] Becquart C S, Domain C, Sarkar U, DeBacker A and Hou M 2010 Microstructural evolution of irradiated tungsten: *ab initio* parameterisation of an OKMC model *J. Nucl. Mater.* **403** 75–88

[142] Dalla Torre J, Bocquet J, Doan N V, Adam E and Barbu A 2005 JERK, an event-based kinetic Monte Carlo model to predict microstructure evolution of materials under irradiation *Phil. Mag.* A **85** 549

[143] Opplestrup T, Bulatov V V, Gilmer G H, Kalos M H and Sadigh B 2006 First-passage Monte Carlo algorithm: diffusion without all the hops *Phys. Rev. Lett.* **97** 230602

[144] Warrier M, Schneider R, Salonen E and Nordlund K 2004 Multi scale modeling of hydrogen isotope diffusion in graphite *Contrib. Plasma Phys.* **44** 307–10

[145] Schneider R, Rai A, Mutzke A, Warrier M, Salonen E and Nordlund K 2007 Dynamic Monte-Carlo modeling of hydrogen isotope reactive-diffusive transport in porous graphite *J. Nucl. Mater.* **367** 1238–42

[146] Warrier M, Schneider R, Salonen E and Nordlund K 2007 Effect of the porous structure of graphite on atomic hydrogen diffusion and inventory *Nucl. Fusion* **47** 1656–63

[147] Henriksson K O E, Nordlund K, Krasheninnikov A and Keinonen J 2006 The depths of hydrogen and helium bubbles in tungsten—a comparison *Fusion Sci. Technol.* **50** 43–57

[148] Rieth M *et al* 2013 Recent progress in research on tungsten materials for nuclear fusion applications in Europe *J. Nucl. Mater.* **432** 482–500

[149] Hull D and Bacon D J 2001 *Introduction to Dislocations* 4th edn (Oxford: Butterworth-Heinemann)

[150] Hirth J P and Lothe J 1992 *Theory of Dislocations* 2nd edn (Malabar, FL: Krieger)

[151] Fitzgerald S P and Aubry S 2010 Self-force on dislocation segments in anisotropic crystals *J. Phys. Condens. Matter* **22** 295403

[152] Fitzgerald S P, Aubry S, Dudarev S L and Cai W 2012 Dislocation dynamics simulation of Frank–Read sources in anisotropic alpha-Fe *Modelling Simul. Mater. Sci. Eng.* **20** 045022

[153] Diaz de la Rubia T, Zbib H M, Khraishi T A, Wirth B D, Victoria M and Caturla M J 2000 Multiscale modelling of plastic flow localization in irradiated materials *Nature* **406** 871–4

[154] Osetsky Yu N, Serra A and Priego V 2000 Interactions between mobile interstitial clusters in Cu and α-Fe *J. Nucl. Mater.* **276** 202–12

[155] Puigvi M A, de Diego N, Serra A, Osetsky Yu N and Bacon D J 2007 On the interaction between a vacancy and self-interstitial atom clusters in metals *Phil. Mag.* **87** 3501

[156] Mordehai D, Fivel M, Clouetab E and Verdier M 2008 Introducing dislocation climb by bulk diffusion in discrete dislocation dynamics *Phil. Mag.* A **88** 899–925

[157] Terentyev D, Klimenkov M and Malerba L 2009 Confinement of motion of interstitial clusters and dislocation loops in bcc Fe–Cr alloys *J. Nucl. Mater.* **393** 30–5

[158] Eyring H 1935 *J. Chem. Phys.* **3** 107

[159] Wigner E 1932 *Z. Phys. Chem. Abt.* **19** 203

[160] Brailsford A and Bullough R 1981 *R. Phil. Trans. R. Soc. Lond.* **302** 87

[161] Doan N and Martin G 2003 *Phys. Rev.* **67** 134107

[162] Reddy J N 2005 *An Introduction to the Finite Element Method* 3rd edn (New York: McGraw-Hill)

[163] Deborst R and Muhlhaus H B 1992 Gradient-dependent plasticity—formulation and algorithmic aspects *Int. J. Numer. Methods Eng.* **35** 521

[164] Kohlhoff S, Gumbsch P and Fischmeister H F 1991 Crack propagation in bcc crystals studied with a combined finite-element and atomistic model *Phil. Mag.* A **64** 851

[165] Tadmor E B, Ortiz M and Phillips R 1996 Quasicontinuum analysis of defects in solids *Phil. Mag.* A **73** 1529

[166] Shenoy V B, Miller R, Tadmor E B, Phillips R and Ortiz M 1998 Quasicontinuum models of interfacial structure and deformation *Phys. Rev. Lett.* **80** 742

J. Phys. D: Appl. Phys. **47** (2014) 224018

K Nordlund *et al*

[167] Masaki K, Kodama K, Ando T, Saidoh M, Shimizu M,
Hayashi T and Okuno K 1996 Tritium retention in graphite
inner wall of JT-60U *Fusion Eng. Des.* **31** 181–7

[168] The Max-Planck Institute for Plasma Physics
www.ipp.mpg.de/ippcms/eng/for/projekte/
w7x/device/divertor/index.html

[169] Roth J, Scherzer B M U, Blewer R S, Brice D K, Picraux S T
and Wampler W R 1980 Trapping, detrapping and
replacement of keV hydrogen implanted into graphite
*J. Nucl. Mater.* **93 & 94** 601–7

[170] Yamashina T and Hino T 1991 Plasma-surface interactions of
graphite as nuclear fusion material *Appl. Surf. Sci.*
**48/49** 483–97

[171] Horn A, Schenk A, Biener J, Winter B, Lutterloh C,
WIttmann M and Küppers J 1994 H atom impact induced
chemical erosion reaction at C : H film surfaces *Chem.
Phys. Lett.* **231** 193–8

[172] Nakamura K, Nagase A, Dairaku M, Akiba M, Araki M and
Okumura Y 1995 Sputtering yields of carbon based
materials under high particle flux with low energy *J. Nucl.
Mater.* **220–2** 890–4

[173] Roth J and García-Rosales C 1996 Analytic description of the
chemical erosion of graphite by hydrogen ions *Nucl.
Fusion* **36** 1647–59
Roth J and García-Rosales C 1997 *Nucl. Fusion* **37** 897
(corrigendum)

[174] Tanihuchi M, Sato K, Ezato K, Yokoyama K, Dairaku M and
Akiba M 2003 Sputtering of carbon–tungsten mixed
materials by low energy deuterium *J. Nucl. Mater.*
**313–16** 360–3

[175] Hopf C, von Keudell A and Jacob W 2003 Chemical
sputtering of hydrocarbon films *J. Appl. Phys.* **94** 2373

[176] Meyer F W, Krause H F and Vergara L I 2005 Measurements
of chemical erosion of ATJ graphite by low energy $D_2^+$
impact *J. Nucl. Mater.* **337–9** 922

[177] Roth J 1981 Chemical sputtering *Sputtering by Particle
Bombardment* vol 1, ed R Behrisch (Berlin: Springer)
pp 91–146

[178] de Juan Pardo E, Balden M, Cieciwa B, Garcia-Rosales C
and Roth J 2004 Erosion processes of carbon materials
under hydrogen bombardment and their mitigation b *Phys.
Scr.* **T111** 62–7

[179] Nordlund K, Salonen E, Keinonen J and Wu C H 2000
Sputtering of hydrocarbons by ion-induced breaking of
chemical bonds *Nucl. Instrum. Methods Phys. Res.* B
**180** 77

[180] Salonen E, Nordlund K, Keinonen J, Runeberg N and
Wu C H 2002 Reduced chemical sputtering of carbon by
silicon doping *J. Appl. Phys.* **92** 2216–8

[181] Träskelin P, Nordlund K and Keinonen J 2006 H, He, Ne,
Ar-bombardment of amorphous hydrocarbon structures
*J. Nucl. Mater.* **357** 1–8

[182] de Rooij E D, von Toussaint U, Kleyn A W and
Goedheer W J 2009 Molecular dynamics simulations of
amorphous hydrogenated carbon under high hydrogen
fluxes *Phys. Chem. Chem. Phys.* **11** 9823

[183] Reinhold C O, Krstic P S, Stuart S J, Zhang H, Harris P R
and Meyer F W 2010 Isotope dependence of chemical
erosion of carbon *J. Nucl. Mater.* **401** 1–12

[184] Alimov V Kh *et al* 1992 Characterization of a-b/C : H films
deposited from different boron containing precursors
*J. Nucl. Mater.* **196–8** 670–5

[185] Kalin B A, Yakushin V L, Polsky V I and Virgilev Yu S 1994
Sputtering of surface-boronized graphite by hydrogen ion
bombardment *J. Nucl. Mater.* **212–15** 1206–10

[186] Wu C H, Alessandrini C, Moormann R, Rubel M and
Scherzer B M U 1995 Evaluation of silicon doped
CFCs for plasma facing material *J. Nucl. Mater*
**220–2** 860–4

[187] Wu C H, Alessandrini C, Bonal P, Caso A, Grote H,
Moormann R, Perujo A, Balden M, Werle H and Vieider G
1997 Evaluation of an advanced silicon doped CFC for
plasma facing material *Fusion Technology 1996*
ed C Varandas and F Serra (Amsterdam: Elsevier)
pp 327–30

[188] Balden M, Roth J and Wu C H 1998 Thermal stability and
chemical erosion of the silicon doped CFC material NS31
*J. Nucl. Mater.* **258–63** 740–4

[189] Grote H, Bohmeyer W, Kornejew P, Reiner H-D,
Fussmann G, Schlögl R, Weinberg G and Wu C H 1999
Chemical sputtering yields of carbon based materials at
high ion flux densities *J. Nucl. Mater.* **266–269** 1059–64

[190] Salonen E, Nordlund K, Keinonen J and Wu C H 2001
Chemical sputtering of amorphous silicon carbide under
hydrogen bombardment *Appl. Surf. Sci.* **184** 387–90

[191] Brezinsek S *et al* and JET-EFDA Contributors 2013 Residual
carbon content in the initial ITER-like wall experiments at
jet *J. Nucl. Mater.* **438** S703

[192] Nordlund K, Salonen E, Krasheninnikov A V and Keinonen J
2006 Swift chemical sputtering of covalently bonded
materials *Pure Appl. Chem.* **78** 1203–12

[193] Nordlund K, Björkas C, Vörtler K, Meinander A, Lasa A,
Mehine M and Krasheninnikov A V 2011 Mechanism of
swift chemical sputtering: comparison of Be/C/W dimer
bond breaking *Nucl. Instrum. Methods Phys. Res.* B
**269** 1257–61

[194] Björkas C, Borodin D, Kirschner A, Janev R K, Nishijima D,
Doerner R and Nordlund K 2012 Molecules can be
sputtered also from pure metals: sputtering of beryllium
hydride by fusion plasma–wall interactions *Plasma Phys.
Control. Fusion* **55** 074004

[195] Lasa A, Björkas C, Vörtler K and Nordlund K 2012 MD
simulations of low energy deuterium irradiation on W, WC
and W2C surfaces *J. Nucl. Mater.* **429** 284–92

[196] Björkas C and Nordlund K 2013 Variables affecting
simulated be sputtering yields *J. Nucl. Mater.*
**439** 174–9

[197] Björkas C, Vörtler K, Nordlund K, Nishijima D and
Doerner R 2009 Chemical sputtering of be due to D
bombardment *New J. Phys.* **11** 123017

[198] Nishijima D, Doerner R P, Baldwin M J, De Temmerman G
and Hollmann E M 2008 Properties of bed molecules in
edge plasma relevant conditions *Plasma Phys. Control.
Fusion* **50** 125007

[199] Björkas C and Nordlund K 2009 Assessment of the relation
between ion beam mixing, electron–phonon coupling, and
damage production in Fe *Nucl. Instrum. Methods Phys.
Res.* B **267** 1830–6

[200] Duxbury G, Stamp M F and Summers H P 1998 Observations
and modelling of diatomic molecular spectra from jet
*Plasma Phys. Control. Fusion* **40** 361

[201] Brezinsek S 2013 *EPS conf. (Espoo)*

[202] Kirschner A, Wienhold P, Phillips V, Coad J P, Huber A,
Samm U and JET EFDA contributors 2004 Modelling of
carbon transport in fusion devices: evidence of enhanced
re-erosion of *in situ* re-deposited carbon *J. Nucl. Mater.*
**328** 62

[203] Björkas C, Borodin D, Kirschner A, Janev R K, Nishijima D,
Doerner R and Nordlund K 2012 Multi-scale modeling of
bed molecular sputtering *J. Nucl. Mater.* **438** S272–5

[204] Luthin J and Linsmeier Ch 2000 Carbon films and carbide
formation on tungsten *Surf. Sci.* **454–6** 78–82

[205] Linsmeier Ch, Luthin J and Goldstrass P 2001 Mixed material
formation and erosion *J. Nucl. Mater.* **290–3** 25–32

[206] Inai K, Kikuhara Y and Ohya K 2008 Comparison of carbon
deposition on tungsten between molecular dynamics and
dynamic Monte Carlo simulation *Surf. Coat. Technol.*
**202** 5374–8

J. Phys. D: Appl. Phys. **47** (2014) 224018

K Nordlund *et al*

[207] Träskelin P, Björkas C, Juslin N, Vörtler K and Nordlund K 2007 Radiation damage in WC studied with MD simulations *Nucl. Instrum. Methods Phys. Res.* B **257** 614

[208] Träskelin P, Juslin N, Erhart P and Nordlund K 2007 Molecular dynamics simulations of hydrogen bombardment of tungsten carbide surfaces *Phys. Rev.* B **75** 174113

[209] Vörtler K, Björkas C and Nordlund K 2010 The effect of plasma impurities on the sputtering of tungsten carbide *J. Phys.: Condens. Matter* **23** 085002

[210] Björkas C, Vörtler K and Nordlund K 2006 Major elemental asymmetry and recombination effects in irradiated WC *Phys. Rev.* B **74** 140103

[211] Petzow G, Aldinger F, Jonsson S and Preuss O 1985 Beryllium and beryllium compounds *Ullmanns Encyclopedia of Industrial Chemistry* vol A4 p 11

[212] Goldstrass P and Linsmeier Ch 2001 Formation of mixed layers and compounds on beryllium due to C and Co bombardment *J. Nucl. Mater.* **290–3** 71–5

[213] Ferro Y, Allouche A and Linsmeier C 2013 Absorption and diffusion of beryllium in graphite, beryllium carbide formation investigated by density functional theory *J. Appl. Phys.* **113** 213514

[214] Sang C, Bonnin X, Warrier M, Rai A, Schneider R, Sun J and Wang D 2012 Modelling of hydrogen isotope inventory in mixed materials including porous deposited layers in fusion devices *Nucl. Fusion* **52** 043003

[215] Roth J 1999 Chemical erosion of carbon based materials in fusion devices *J. Nucl. Mater.* **266–9** 51–7

[216] Balasubramanian K 2000 Spectroscopic constants and potential energy curves of tungsten carbide *J. Chem. Phys.* **112** 7425

[217] Meinander A, Björkas C and Nordlund K 2013 The effect of hydrocarbon chemistry on sputtering in mixed Be–C–H materials *Nucl. Instrum. Methods Phys. Res.* B **303** 188

[218] Heinola K, Ahlgren T, Vainonen-Ahlgren E, Likonen J and Keinonen J 2007 *Phys. Scr.* T **128** 91

[219] Ahlgren T, Heinola K, Vörtler K and Keinonen J 2012 *J. Nucl. Mater.* **427** 152

[220] Alimov V K, Roth J, Causey R, Komarov D, Linsmeier C, Wiltner A, Kost F and Lindig S 2008 *J. Nucl. Mater.* **375** 192

[221] Zhou H-B, Liu Y-L, Jin S and Zhang Y 2010 *Nucl. Fusion* **50** 025016

[222] Haasz A, Poon M, Macaulay-Newcombe R and Davis J 2001 *J. Nucl. Mater.* **290–293** 85

[223] Matsui T, Muto S and Tanabe T 2000 *J. Nucl. Mater.* **283–287** 1139

[224] Sakamoto R, Muroga T and Yoshida N 1995 Microstructural evolution induced by low energy hydrogen ion irradiation in tungsten *J. Nucl. Mater.* **220–222** 819

[225] García-Rosales C, Franzen P, Plank H, Roth J and Gauthier E 1996 Re-emission and thermal desorption of deuterium from plasma sprayed tungsten coatings for application in ASDEX-Upgrade *J. Nucl. Mater.* **233–237** 803

[226] Pisarev A A, Voskresensky I D and Porfirev S I 2003 Computer modeling of ion implanted deuterium release from tungsten *J. Nucl. Mater.* **313–316** 604

[227] Wright G M, Brunner D, Baldwin M J, Doerner R P, Labombard B, Lipschultz B, Terry J L and Whyte D G 2012 Tungsten nano-tendril growth in the Alcator C-Mod divertor *Nucl. Fusion* **52** 042003

[228] Kajita S, Sakaguchi W, Ohno N, Yoshida N and Saeki T 2009 Formation process of tungsten nanostructure by the exposure to helium plasma under fusion relevant plasma conditions *Nucl. Fusion* **49** 095005

[229] Baldwin M J, Lynch T C, Doerner R P and Yu J H 2011 Nanostructure formation on tungsten exposed to low-pressure rf helium plasmas: a study of ion energy threshold and early stage growth *J. Nucl. Mater.* **415** S104–7

[230] Baldwin M J, Doerner R P, Nishijima D, Tokunaga K and Ueda Y 2009 The effects of high fluence mixed-species (deuterium, helium, beryllium) plasma interactions with tungsten *J. Nucl. Mater.* **390–1** 886–90

[231] Krasheninnikov S I 2011 Viscoelastic model of tungsten 'fuzz' growth *Phys. Scr.* **T145** 014040

[232] Sharafat S, Takahashi A, Nagasawa K and Ghoniem N 2009 A description of stress driven bubble growth of helium implanted tungsten *J. Nucl. Mater.* **389** 203–12

[233] Martynenko Yu V and Nagel M Yu 2012 Model of fuzz formation on a tungsten surface *Plasma Phys. Rep.* **38** 996–9

[234] Lasa A, Tähtinen S K and Nordlund K 2014 Loop punching and bubble rupture causing surface roughening—a model for W fuzz growth *Europhys. Lett.* **105** 25002

[235] Baldwin M J and Doerner R P 2010 Formation of helium induced nanostructure 'fuzz' on various tungsten grades *J. Nucl. Mater.* **404** 165–73

[236] Becquart C S, Souidi A, Domain C, Hou M, Malerba L and Stoller R E 2006 Effect of displacement cascade structure and defect mobility on the growth of point defect clusters under irradiation *J. Nucl. Mater.* **351** 39

[237] Becquart C S and Domain C 2007 *Ab initio* calculations about intrinsic point defects and He in W *Nucl. Instrum. Methods Phys. Res.* B **255** 23–6

[238] Becquart C S and Domain C 2009 A density functional theory assessment of the clustering behaviour of He and H in tungsten *J. Nucl. Mater.* **386–8** 109–11

[239] Becquart C S and Domain C 2009 An object kinetic Monte Carlo simulation of the dynamics of helium and point defects in tungsten *J. Nucl. Mater.* **385** 223–7